

Outflows from GRB hosts are ubiquitous: Kinematics of $z < 0.3$ GRB-SN hosts resolved with FLAMES [★]

C. C. Thöne¹, L. Izzo^{1,3}, H. Flores², A. de Ugarte Postigo^{1,3}, S. D. Vergani², J. F. Agüí Fernández¹, D. A. Kann¹, L. Christensen³, S. Covino⁴, M. Della Valle⁵, F. Hammer², A. Melandri⁴, M. Puech², M. A. Rodrigues⁶, and J. Gorosabel^{1,7,8†}

¹ Instituto de Astrofísica de Andalucía - CSIC, Glorieta de la Astronomía s/n, 18008 Granada, Spain
e-mail: cthoene@iaa.es

² GEPI, Observatoire de Paris, PSL University, CNRS, 5 Place Jules Janssen, 92190 Meudon, France

³ Dark Cosmology Centre, Niels-Bohr-Institute, Univ. of Copenhagen, Jagtvej 128, 2200 Copenhagen

⁴ INAF, Osservatorio Astronomico di Brera, Via Bianchi 46, 23807 Merate (LC), Italy

⁵ Astronomical Observatory of Capodimonte in Naples (OACN), Salita Moiariello, Napoli, 80131, Italy

⁶ University of Oxford, Department of Physics, Keble Road, Oxford OX1 3RH, UK

⁷ Departamento de Física Aplicada I, E.T.S. Ingeniería, Universidad del País-Vasco UPV/EHU, Alameda de Urquijo s/n, 48013 Bilbao, Spain

⁸ Ikerbasque, Basque Foundation for Science, Alameda de Urquijo 36-5, 48008 Bilbao, Spain

Received ; accepted

ABSTRACT

The hosts of long duration gamma-ray bursts (GRBs) are predominantly starburst galaxies at subsolar metallicity. At redshifts $z < 1$, this implies that most of them are low-mass galaxies similar to the populations of blue compact dwarfs and dwarf irregulars. What triggers the massive star-formation needed for producing a GRB progenitor is still largely unknown, as are the resolved gas properties and kinematics of these galaxies and their formation history. Here we present a sample of six spatially resolved GRB hosts at $z < 0.3$ observed with 3D spectroscopy at high spectral resolution ($R = 8,000\text{--}13,000$) using FLAMES/VLT. We analyzed the resolved gas kinematics of the full sample and the abundances in a subsample with strong enough emission lines. Only two galaxies show a regular disk-like rotation field, another two are dispersion-dominated, and the remaining ones have two narrow emission components associated with different parts of the galaxy but no regular rotation field, which might indicate a recent merger. All galaxies show evidence for broad components underlying the main emission peak with σ of $50\text{--}110\text{ km s}^{-1}$. This broad component is more metal-rich than the narrow components, it is blueshifted in most cases, and it follows a different velocity structure. We find a weak correlation between the star-formation rate and the width of the broad component, its flux compared to the narrow component, and the maximum outflow velocity of the gas, but we do not find any correlation with the star-formation density, metallicity or stellar mass. We hence associate this broad component with a metal-rich outflow from star-forming regions in the host. The GRB is not located in the brightest region of the host, but is always associated with some star-forming region showing a clear wind component. Our study shows the great potential of 3D spectroscopy to study the star-formation processes and history in galaxies hosting extreme transients, the need for high signal-to-noise (S/N), and the perils using unresolved or only partially resolved data for these kinds of studies.

Key words. stars: gamma-ray bursts, galaxies: kinematics and dynamics, galaxies: starbursts

1. Introduction

Long gamma-ray burst (LGRB) progenitors have indubitably been identified as massive stars through their connection to broad-line Type Ic supernovae (SNe) coincident with the GRB (for a recent review see Cano et al. 2017). Models suggest that their progenitors are Wolf-Rayet (WR) stars, massive stars stripped of their H and He envelopes, with low metallicity where stellar winds are weaker, and they retain enough angular momentum necessary for the GRB jet to form (Woosley & Heger 2006). Massive star-formation in low metallicity gas at low redshift happens primarily in dwarf starburst galaxies. Unsurprisingly, dwarf galaxies dominate the population of low redshift GRB hosts: The average luminosity and stellar masses of GRB hosts are -19 mag or $\log M^* = 9.0 M_\odot$ at $z \approx 0$, but they rise to $\log M^* = 9.6 M_\odot$ and $>10 M_\odot$ at redshifts of $1 < z < 2$ and $z > 2$ (Perley et al. 2016;

Palmerio et al. 2019). GRB hosts at low redshift are similar to the galaxy populations of blue compact dwarfs (BCDs, defined as $M_{\text{abs}} < -18\text{ mag}$ and size $< 1\text{ kpc}$), and dwarf irregulars (dIrrs); a few have also been found to be dwarf spiral galaxies (e.g., GRB 980425 and GRB 060505). A few exceptions are GRB 171205A, the third closest GRB ever detected and hosted by a large spiral with a mass of $\log M^* \sim 10.1$ (Perley & Taggart 2017; Izzo et al. 2019; Thöne et al. in prep.), the even larger spiral host of GRB 190829A (Izzo et al. in prep.) and the more distant face-on grand design spiral host of GRB 990705 (Le Flocc’h et al. 2002; Hunt et al. 2014).

Since GRBs are distant and occur in small galaxies rarely monitored by high angular-resolution surveys, it is unlikely for the foreseeable future to image the progenitor of a GRB, hence we need to infer properties of the progenitor star from its environment. The average redshift of LGRBs is $z \sim 2.2$ (Coward et al. 2013) where 1 arcsec corresponds to a physical size of 8 kpc,

[★] based on ESO proposal 092.D-0389, PI C. Thöne

preventing spatially resolved observations with current facilities. To date only a handful of GRB hosts have been studied with IFU data: GRB 980425 (Christensen et al. 2008; Krühler et al. 2017), the SN-less long GRB 060505 (Thöne et al. 2008, 2014), GRB 100316D (Izzo et al. 2017), which contains one of the datasets presented in this paper, and GRB 111005A, another potential SN-less GRB (Tanga et al. 2018; Michałowski et al. 2018).

The origin of star-formation in dwarf galaxies is still largely unknown. Their star-burst episodes seem to only last a few tens of Myr followed by Gyrs of quiescence (Lee et al. 2009; McQuinn et al. 2010; Zhao et al. 2011). The small potential well allows to disrupt molecular clouds with only a few SN explosions and quench SF. Some starbursts might be triggered by interactions (see e.g., Bekki 2008; van Zee et al. 1998), suggestions are up to >60% (Pérez-Gallego et al. 2011), but many galaxies seem to be isolated (see e.g. the SIGRID sample, Nicholls et al. 2014, or the LITTLE THINGS survey, Hunter et al. 2012). However, low luminosity neighbors may easily go undetected and only show up in HI gas (see e.g. Ashley et al. 2013, 2017). Other possible mechanisms include inflows of gas (Elmegreen & Hunter 2015; Verbeke et al. 2014), or stellar feedback and ram-stripping, removing gas that is later re-accreted (Ashley et al. 2017). Very likely not one single mechanism can explain all starburst activity in dwarf galaxies (see e.g. Koleva et al. 2014).

GRB hosts are only rarely found to be interacting systems (e.g. GRB 090323, Savaglio et al. 2012, GRB 090426, Thöne et al. 2011, GRB 120422A, Schulze et al. 2014, GRB 080810, Wiseman et al. 2017, and possibly GRB 060418 and GRB 050820, Chen 2012). Inflows have been suggested as a SF trigger from resolved HI and radio continuum maps (Michałowski et al. 2012, 2015). HI might also trace past interactions [e.g. for the host of GRB 980425] (Arabsalmani 19). Even in the most compact dwarfs, kinematics of hot gas, HI gas and stellar kinematics do not necessarily trace each other, supporting the interaction scenario for star-formation (Johnson et al. 2012; Koleva et al. 2014; Ashley et al. 2017).

Star-burst dwarf galaxies often show broad components in nebular emission lines with velocities up to a thousand km s^{-1} (Izotov et al. 2007; Telles et al. 2014). Possible explanations are 1) SN explosions or stellar winds form large bubbles (Telles et al. 2014), 2) turbulent mixing layers on the surface of dense gas clouds (Westmoquette et al. 2007; James et al. 2009) or 3) AGN activity, although the latter has been mostly ruled out (Izotov et al. 2007; James et al. 2009). Green-pea (GP) galaxies (Cardamone et al. 2009), extreme BCDs in an early starburst phase characterized by strong [OIII] emission, often show broad components associated with SN driven winds (Amorín et al. 2012). The frequency of these components in the starburst galaxy population is still a matter of debate (see e.g. James et al. 2010).

Galactic winds are linked to starburst activity. At low redshift they can be directly observed (e.g. in M82) while at high redshifts they are studied via absorption lines (for reviews see Veilleux et al. 2005; Rupke 2018). Emission and absorption lines probe different parts of the winds, but beyond the local Universe, observing both has rarely been done (Erb et al. 2012; Wood et al. 2015). Recently, the MEGAFLOW sample began to study galactic winds detected in background QSO absorbers and their galaxy counterparts in emission with MUSE (Schroetter et al. 2016; Zabl et al. 2020). Galactic winds are now seen as a crucial factor in explaining and constraining the shape of the mass-metallicity relation (Mannucci et al. 2010; Chisholm et al. 2018) and the enrichment of the intergalactic medium (IGM).

In this paper we present the first sample of long GRB hosts observed at high spatial and spectral resolution with

FLAMES/VLT which is complete up to $z = 0.3$ for GRBs discovered until early 2013 and observable from the VLT. This comprises the hosts of GRB 020903, GRB 030329, GRB 031203, GRB 050826, GRB 060218, GRB 100316D and GRB 120422A. For GRB 120422A, we did not obtain data due to an incorrect pointing of the instrument. In Sect. 2 we present the observations and analysis, Sect. 3 details the result for the different hosts regarding kinematics and abundances and Sect. 4 discusses the results. Throughout the paper we use a flat lambda CDM cosmology as constrained by Planck with $\Omega_m = 0.315$, $\Omega_\Lambda = 0.685$ and $H_0 = 67.4$ (Planck Collaboration et al. 2020).

2. Observations and analysis

The GRB host sample was observed with FLAMES/GIRAFFE at the VLT between Nov. 2013 and March 2014 with a total observing time of 22 h. Observations were done in ARGUS mode with the 0.3" sampling size, which provides a $6.6'' \times 4.2''$ field-of-view (FOV, see Fig. 1). We used the low resolution grating at three different incidence angles called LR6, 7 and 8, resulting in spectral resolutions of $R = 13,500$, 8200 and 10,000 respectively. The aim was to cover at least the range from $H\alpha$ to [SII] at the different redshifts of the galaxies. The exact wavelength coverage for each spectrum is shown in Fig. 2.

The nominal seeing varies as observations were performed at different dates. The values are 0.7" for GRB 020903 and GRB 030329, 0.8" for GRB 031203 and GRB 100316D, 1.0" for GRB 050826 and 1.2" for GRB 060218. The ARGUS data reduction was done using the standard ESO pipeline (version 2.11) without the sky subtraction option. To verify the fiber-to-fiber wavelength calibration, we controlled the wavelength of two skylines in the data cube. No absolute flux calibration was performed.

The sample was analyzed with dedicated software in IDL and IRAF, partially based on tools presented in Flores et al. (2006); Yang et al. (2008). For the emission line maps we integrated the flux over the emission line and subtracted the continuum from a line-free region around the emission line. This approach was chosen since the emission lines have shapes often deviating from a pure Gaussian. To obtain the velocity maps we fit $H\alpha$ with a single Gaussian, even if several components are present, hence this shows the properties of the dominant line component. Using several sky emission lines we derive an instrumental resolution of $\text{FWHM} = 39.9 \text{ km s}^{-1}$ (σ of 16.9 km s^{-1}). The dispersion σ is corrected for the instrumental resolution by subtracting it in quadrature. All maps are interpolated to $\sim 0.02''$ for better visualization. Multicomponent fits to individual emission lines for kinematical analysis were done with `ngaussfit` in IRAF and PAN in IDL (Peak ANalysis, Dimeo 2005; Westmoquette et al. 2007). The final maps are plotted in Fig. 1.

Metallicities were obtained using the N2-parameter $[\text{N II}]\lambda 6585/H\alpha$ taking the recalibration from the CALIFA sample (Marino et al. 2013). Relative line fluxes for [NII] and $H\alpha$ were derived from a single Gaussian fit, due to their proximity in wavelength, an absolute flux calibration is not needed to derive the ratio of the two lines.

3. Results of the individual hosts

In Fig. 2 we plot the integrated spectra of the galaxies in the sample. $H\alpha$ is detected in all galaxies while the detection of further lines depends on the S/N of the spectra. Only for two hosts, GRB 031203 and GRB 100316D, are we able to obtain 2D maps of emission line ratios and abundances. In the following we give

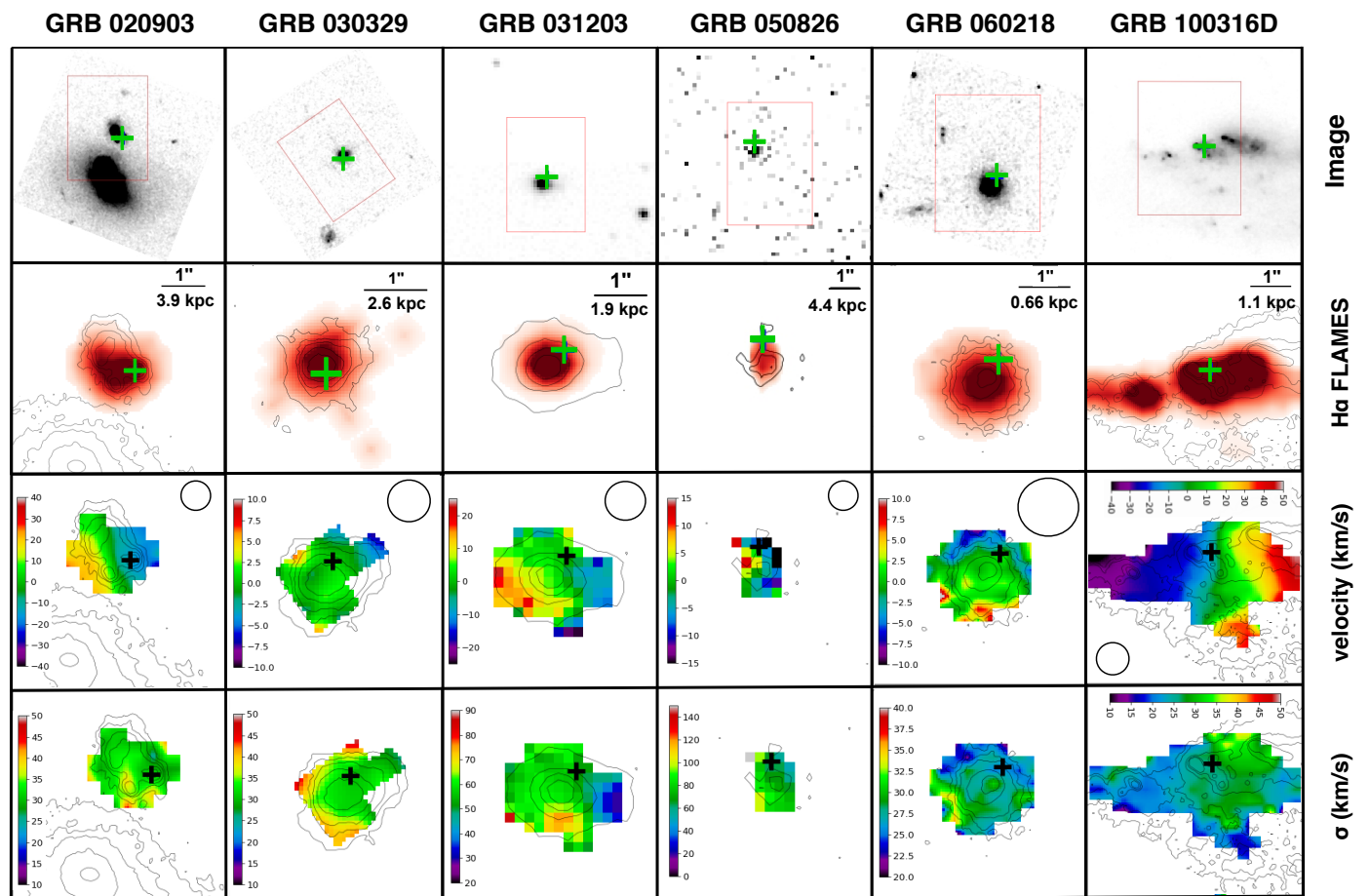


Fig. 1. GRB hosts observed with FLAMES. *Top row:* Imaging of the field, the position of the GRB is marked by a green cross, the FLAMES FOV is shown by a red rectangle. Images are from HST for GRB 020903, GRB 030329, GRB 060218 and GRB 100316D (Fruchter et al. 2006; Svensson et al. 2010). For GRB 050826 we used data from the PanSTARRS survey, for GRB 031203 imaging from FORS 2/VLT from the ESO archive. *Second row:* H α maps interpolated to $\sim 0.02''$ for better visualization with contours overplotted using the broad-band image in the top row. *Third and fourth row:* Velocity and dispersion maps of the sample derived from a single Gaussian fit to H α . The maps are interpolated to the resolution of the image used for the contour plot ($0.02''$ for the ones with HST imaging, $0.25''$ for the FORS and PanSTARRS images of the hosts of GRB 031203 and GRB 050826). The nominal resolution including the seeing is shown by a circle for each host. In all plots north is up and east is left.

a brief overview of literature results for each GRB host and the detected emission lines after which we focus on the kinematic analysis and the resolved abundances for those two hosts where this has been possible.

3.1. GRB 020903

The host at $z = 0.251$ is an irregular galaxy with either several SF regions or an interacting system as can be seen in HST images of the host (Fruchter et al. 2006; Svensson et al. 2010) (see the contours in Fig. 1). The galaxy is small with r_{80} of 1.43 kpc, has a stellar mass of $\log M^* = 8.87 M_{\odot}$ and a SFR of $1.7 M_{\odot} \text{ yr}^{-1}$ (Svensson et al. 2010; Levesque et al. 2010a). Han et al. (2010) found a tentative detection of Wolf-Rayet (WR) features in this galaxy. Levesque et al. (2010a) also found a high ionization parameter for this galaxy indicative of a hard radiation field, which is not surprising given the presence of WR stars.

We only detect H α in the FLAMES data, albeit with high S/N, and weak lines of [S II] in the integrated spectra. [N II] is not detected and we get a limit of $12 + \log(O/H) < 8.1$ for the N2 metallicity, in agreement with a metallicity of 7.98 - 8.07 found

by Levesque et al. (2010b) and also the limit derived by Bersier et al. (2006).

The galaxy is next to a system of two larger, interacting galaxies, however, as noted already by Soderberg et al. (2004) they are at a redshift of $z = 0.23$ compared to $z = 0.25$ of the host galaxy ($\Delta v \sim 3900 \text{ km s}^{-1}$) and hence not interacting with the host. At first sight the host of GRB 020903 seems to have a regular rotation curve with a Δv of $\sim 60 \text{ km s}^{-1}$. The line width varies very little across the galaxy (see Fig. 1), only the HII region east of the GRB region has a slightly higher value.

The emission line shows a slight asymmetry which we fit with a double narrow Gaussian profile. The ratio of the two profiles varies across the galaxy and seems to be associated with different parts of the galaxy (see Fig. 3): The bluer component is related to the complex of SF regions in the north of the galaxy while the redder component is associated with the two SF regions in the South, one of which is the GRB region. The combination of these two components and their gradually varying relative strength across the galaxy give the appearance of an ordered rotation field, however, the velocity varies linearly across the FOV (see Fig. 1), which is not expected for a rotating disk.

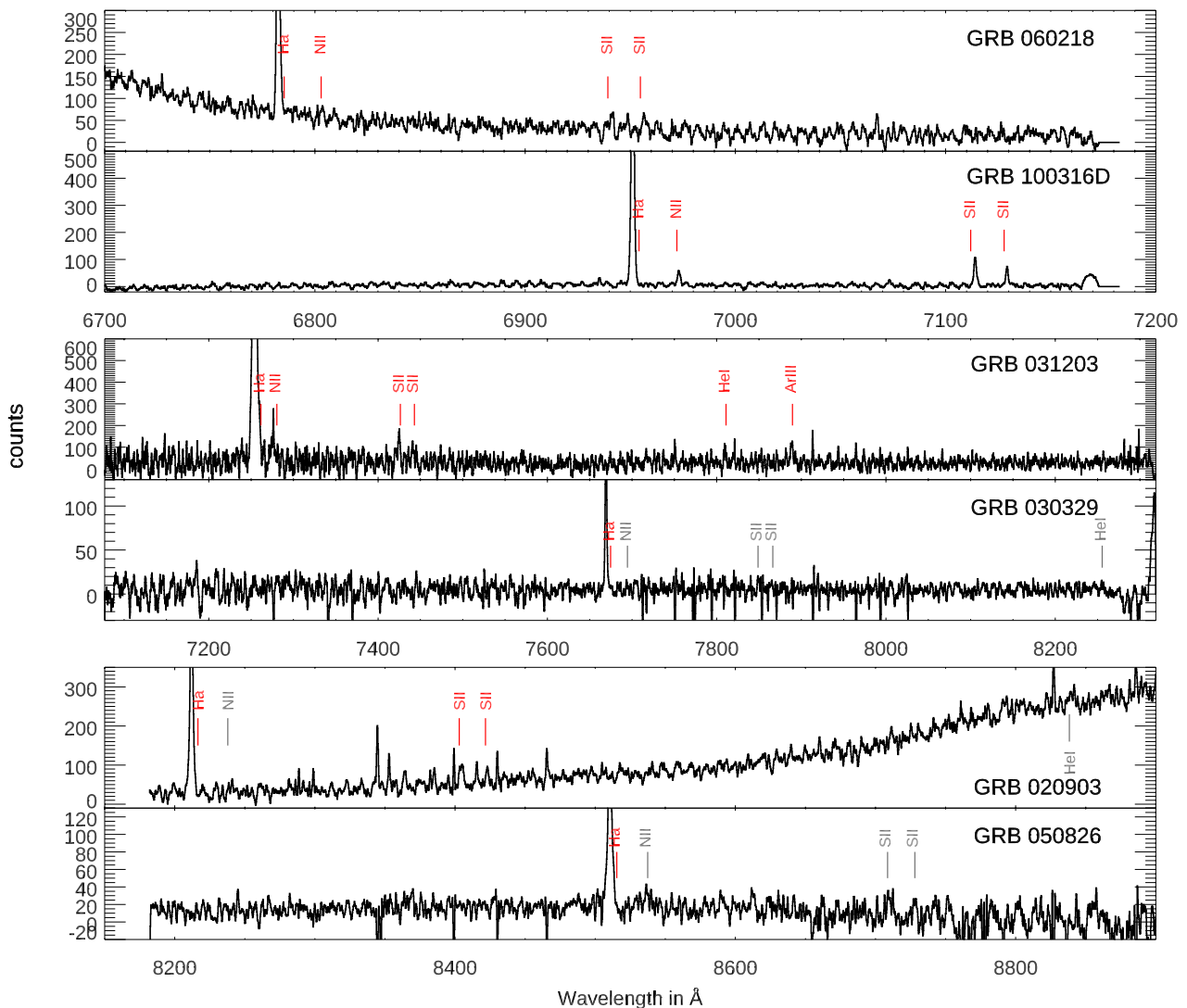


Fig. 2. Integrated spectra of the 6 galaxies in our sample, grouped by the different grating settings used (top to bottom: LR 6, 7 and 8). Red lines are detected transitions, gray tick marks indicate the position of emission lines that are not detected in that particular host. For each spectrum we summed the flux for all regions where H α is detected and subtracted the average sky background using at least 9 spaxels outside the host galaxy. The final spectra have been smoothed with a Gaussian kernel of 5.

Table 1. GRB host sample global properties.

GRB	z	$\log M^*$	M_B	r_{80}	r_{50}	d_{GRB}	SFR	SSFR	ΣSFR	12+log(O/H)	
		M_{\odot}								mag	kpc
020903	0.251	8.94	-19.34	1.43 ^e	0.91	1.1	0.45	0.92	0.070	<8.1	7.98–8.07 ^a
030329	0.169	7.70	-16.52	1.03 ^e	0.54 ⁱ	1.0	0.14	4.74	0.042	<8.0	7.7–8.0 ^{b,c,d}
031203	0.106	8.86	-18.52	1.79	1.04 ⁱ	1.1	4.3	2.48	0.094	8.1	8.1 ^c
050826	0.297	9.99	-20.28	6.21	3.88	3.1	1.39 ^e	0.17	0.03	<8.45	8.8 ^a
060218	0.033	7.40	-15.92	0.55 ^e	0.37 ⁱ	0.5	0.05	1.82	0.053	<7.88	7.6 ^f
100316D	0.059	9.39	-18.8 ^d	3.96	2.55 ⁱ	0.6	1.2 ^h	1.41	0.024	8.25	8.0–8.2 ^{g,h}

Notes. Stellar masses have been obtained by fitting CIGALE (Boquien et al. 2019) SED models to available photometry from the literature (see Appendix). B-band luminosities are from Svensson et al. (2010) based on literature photometry (see that paper for details). For GRB 031203, GRB 050826 and GRB 100316D we derived r_{80} , for GRB 020903 and GRB 050826 r_{50} from FORS2, PanSTARRS and HST imaging used for the contours in Fig.1, the remaining values are from Svensson et al. (2010) and Japelj et al. (2018). d_{GRB} is the distance of the GRB location from the spaxel containing the brightest H α emission. SFRs are based on UV luminosities and taken from Michałowski et al. (2015) when not indicated differently, SSFRs are the SFR divided by the stellar mass, SFR densities are calculated as $\Sigma\text{SFR}=\text{SFR}/(\pi r_{80}^2)$. Metallicities are from the global host spectra using the N2 parameter and the Marino et al. (2013) calibration.

References. ^(a) Levesque et al. (2010b), ^(b) Thöne et al. (2007), ^(c) Levesque et al. (2010a), ^(d) Starling et al. (2012), ^(e) Svensson et al. (2010), ^(f) Wiersema et al. (2007), ^(g) Levesque et al. (2011), ^(h) Izzo et al. (2017), ⁽ⁱ⁾ Japelj et al. (2018).

Table 2. GRB host sample global kinematical properties.

GRB	Δv km s ⁻¹	σ_{int} km s ⁻¹	σ_0 km s ⁻¹	$\log M_{\text{dyn,rot}}$ M _⊙	$\log M_{\text{dyn},\sigma}$ M _⊙	$\log M^*$ M _⊙	v_{esc} km s ⁻¹
020903	59	34	28.4	8.54	8.96	8.94	78
030329	15	27	27.9	7.09	8.72	7.70	70
031203	53	39	11.7	8.51	8.61	8.86	47
050826	43	55	71.6	8.90	10.3	9.99	172
060218	23	24	22.2	7.49	8.43	7.40	68
100316D	92	31	19.4	9.59	9.19	9.39	61

Notes. Δv are the difference between minimum and maximum velocity in the 2D velocity map, $v_{\text{rot}}=0.5\Delta v$ is also called v_{shear} (see Sect. 4.1). σ_{int} is derived from a single Gaussian fit to the integrated spectra of each galaxy. σ_0 is the flux weighted dispersion of H α of all spaxels with sufficient S/N in H α (see Herenz et al. 2016). The FOV of the host of GRB 100316D does not comprise the entire galaxy. Dynamical masses are derived from Δv , σ_0 , r_{80} and r_{50} (see Tab. 1), the escape velocity of the galaxy is derived from the dynamical mass used for the respective systems. For the calculations of $M_{\text{dyn,rot}}$, $M_{\text{dyn},\sigma}$ and v_{esc} see Sect. 4.1).

Table 3. Results of the multicomponent fits for the entire galaxy and different integrated regions in some of the galaxies.

GRB	region	Component 1 (narrow)		Component 2 (narrow)		Component 3 (broad)		EW	F _B /F _N	V _{max}
		δv km s ⁻¹	σ km s ⁻¹	δv km s ⁻¹	σ km s ⁻¹	δv km s ⁻¹	σ km s ⁻¹			
GRB 020903	main SF reg.	3.6	18.2	40.2	22.2	-10.9	58.1	-59±2	0.46	53
	GRB reg.	-40.2	18.2	-7.3	18.2	-18.3	54.9	-61±3	0.36	46
	second SF reg.	-7.3	18.2	21.9	24.1	7.3	51.6	-35±2	0.50	49
	galaxy	-7.3	20.2	25.6	24.1	-18.3	54.9	-62±3	0.64	56
GRB 030329	galaxy	0	21.6	-	-	-74/+70	unres./39.4	-13±2	0.14	24
GRB 031203	center	0	36.7	-	-	-32.2	105.8	-159±3	1.42	94
	GRB reg.	-1.9	35.3	-	-	-28.5	102.2	-255±3	1.31	94
	broad reg.	7.0	36.3	-	-	-26.8	111.9	-182±2	1.79	99
	narrow reg.	-13.3	27.2	-	-	-31.0	103.9	-152±4	1.27	106
GRB 050826	galaxy	-44.1	22.5	22.9	17.9	-19.4	86.3	-25±3	1.03	75
	North/GRB	-31.7	18.0	27.5	5.0	-7.1	75.7	-13±1	0.99	62
	center	-28.2	22.6	28.2	22.6	-7.1	75.7	-12±0.5	0.88	62
	South	-21.2	22.6	38.8	22.6	0	72.0	-9±0.3	0.71	62
GRB 060218	galaxy	0	11.3	-24.8	17.5	-63.3	40.9	-27±5	0.30	13
GRB 100316D	Integ. 1	-15.6	5.6	-	-	-11.2	50.4	-25±1	0.59	67
	Integ. 2	-11.2	10.0	-	-	0	44.5	-44±0.5	0.23	64
	Integ. 3/GRB	0	16.8	-	-	0	44.5	-184±2	0.20	60
	Integ. 4	44.9	16.8	-	-	29.8	39.6	-55±1	0.33	36
	galaxy	-3.0	19.3	-	-	12.0	44.5	-55±2	0.34	71

Notes. The naming of the regions in the different hosts follows the one outlined in the line fitting plots, see Sect. 3. We also list the H α EWs derived from the total line flux in each region and the flux ratio between narrow and broad component F_B/F_N. For GRBs 020903 and 050826 we add the two narrow components for the total F_{narrow}, for GRBs 030329 and 060218 we add the two components in the wings for the total F_{broad}. V_{max} is defined in Sect. 4.4 as $\text{abs}(\Delta v(\text{narrow-broad}) - 0.5 \text{FWHM}_{\text{broad}})$ (see e.g. Veilleux et al. 2005; Arribas et al. 2014). For GRB 020903 and 050826 we use $\Delta v(\text{narrow-broad})$ between the bluest narrow and the broad component, for GRB 030329 we use the blue shifted additional component.

Alternatively, this smoothly varying pattern could be indicative of an outflow along the WNW-ESE direction or an indication of a bar-like rotation.

In addition to the two narrow components, the line shows some excess emission in the blue wing which we fit with a weak broad component (see Fig. 3). This component is most prominent in the part we call “main SF region” but less at the GRB site and the SF region next to the GRB site.

3.2. GRB 030329

The host is a compact, low mass ($\log M^*=7.74 M_{\odot}$, $r_{80} = 1.03$ kpc, Svensson et al. 2010) and low metallicity dwarf ($12+\log(\text{O}/\text{H}) = 7.7 - 8.0$, Thöne et al. 2007; Levesque et al. 2010a; Starling et al. 2012.) Even in high resolution HST images, the host seems to consist of a single SF region (see Fig. 1). Östlin et al. (2008) determined a low age of 5 Myr for the stellar population at the GRB site (assuming an instantaneous star-

burst) using high spatial resolution broad-band data from HST. Levesque et al. (2010a) detect the Balmer series down to H8 together with [NeIII] emission, pointing to a young stellar population. The detection of [OIII] λ 4363 Å, which becomes very faint above $12+\log(\text{O}/\text{H}) > 8.0$, confirms a very low metallicity for this galaxy.

We only detect H α both in individual spaxels and the integrated spectrum. [N II] is too weak at the metallicity of the host and the [S II] doublet is contaminated by bright sky emission lines. He I 7065 would be in the observed spectral range but is not detected. This host, together with the host of GRB 060218, is one of only two GRB hosts where high resolution data of both absorption and emission lines are available.

The host of GRB 030329 has the smallest Δv of all the sample (15 km s⁻¹) and a uniform dispersion across the host. The S/N in the individual spaxels is too low to distinguish different components. In Fig. 4 we fit the H α profile of the integrated galaxy spectrum using both a single Gaussian and two additional com-

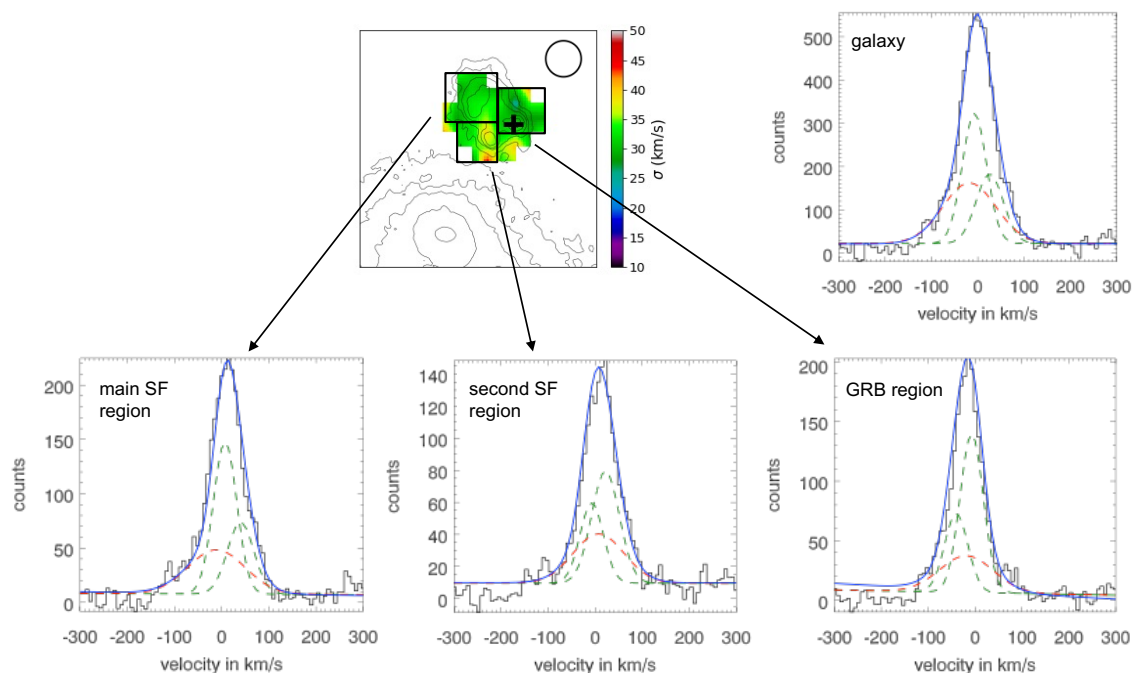


Fig. 3. GRB 020903: Fits to $H\alpha$ for the GRB region, the main SF region, the SF region next to the GRB region and the entire galaxy. The circle in the σ plot shows its nominal resolution.

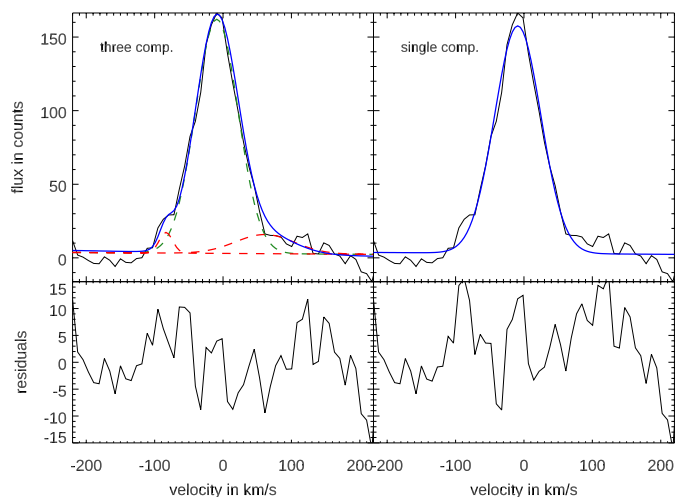


Fig. 4. $H\alpha$ fits and residuals for the host of GRB 030329 using either a combination of a broad and a narrow component (left) or a single Gaussian (right).

ponents in the blue and red wing of the line at velocities of -74 and $+70 \text{ km s}^{-1}$. There is a clear excess of emission in the blue wing, which seems to be present also in individual spaxels. The profile is slightly asymmetric with more emission in the blue part of the Gaussian, however, the data have too low S/N to constrain this further.

Kinematics of the host had previously been analyzed in Thöne et al. (2007) using longslit UVES/VLT spectra of the GRB afterglow. In those spectra, the emission lines show only a single Gaussian component while the absorption lines of Mg I and M II span over 200 km s^{-1} in velocity, blue-shifted compared to the emission line. This has been taken as a strong indication for a starburst wind in this galaxy. The possible excess

emission in the wings of $H\alpha$ found in the FLAMES data would support this conclusion. Any faint component in the wings would have been missed in the UVES data as the afterglow continuum was still bright.

3.3. GRB 031203

The host is a compact, but luminous galaxy ($\log M^* = 8.82 M_\odot$), and has been observed at many wavelengths in multiple studies. Prochaska et al. (2004) found a high extinction corrected SFR of $11 M_\odot \text{ yr}^{-1}$. The GRB was located near the galaxy center in the brightest region of the host. No individual SF regions have been identified and there are no HST images available. The galaxy hosts a young stellar population, indicated by the lack of a 4000 \AA bump and the detection of high excitation MIR lines of Ne II+Ne III and [S III]+[S IV] (Watson et al. 2011). Tentative WR lines have been detected (Han et al. 2010). Strong IR emission points to significant extinction but a high dust temperature ($\sim 70\text{K}$) and the dust-to-stellar mass ratio is smaller than for other bright IR galaxies, suggesting dust properties different from local dwarfs (Symeonidis et al. 2014). Michałowski et al. (2015) detected radio emission but offset toward the west of the galaxy and with a flat spectral slope suggesting a contribution from synchrotron self-absorption, indicative for a very young stellar population. The spectral slope rules out an AGN contribution, contrary to what was suggested by Levesque et al. (2010a).

We detect several emission lines even in individual spaxels: $H\alpha$, [N II], the [S II] doublet, [Ar III] $\lambda 7136$ and He I $\lambda 7065$. The other two He I transitions $\lambda 6678$ and 7221 \AA are not detected, nor is the [O II] $\lambda 7230, 7330$ doublet. All of these lines were detected in X-shooter spectra of the host (Guseva et al. 2011; Watson et al. 2011). In Fig. 6 we plot the line maps together with the ratio of [S II]/ $H\alpha$, the metallicity as well as [Ar III]/ $H\alpha$ and He I/ $H\alpha$. The lines all show a very similar distribution in flux with ratios varying by less than 0.3 dex.

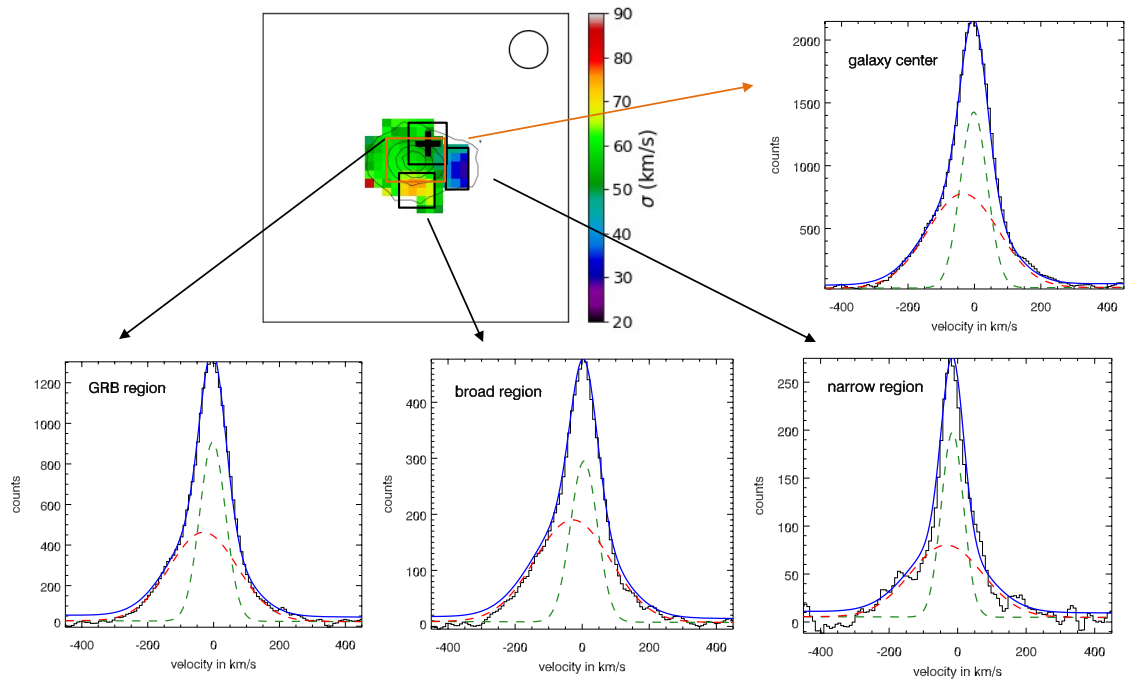


Fig. 5. GRB 031203: Fits to $H\alpha$ for the GRB region, the region of high dispersion (“broad region”) and low dispersion velocity (“narrow region”) as seen in the dispersion map of the host. We add the profile of the integrated spectrum of the brightest 5×6 spaxels in the galaxy center (orange rectangle) which we use for further comparison to X-shooter spectra of the host (see text). The circle in the σ plot shows its nominal resolution.

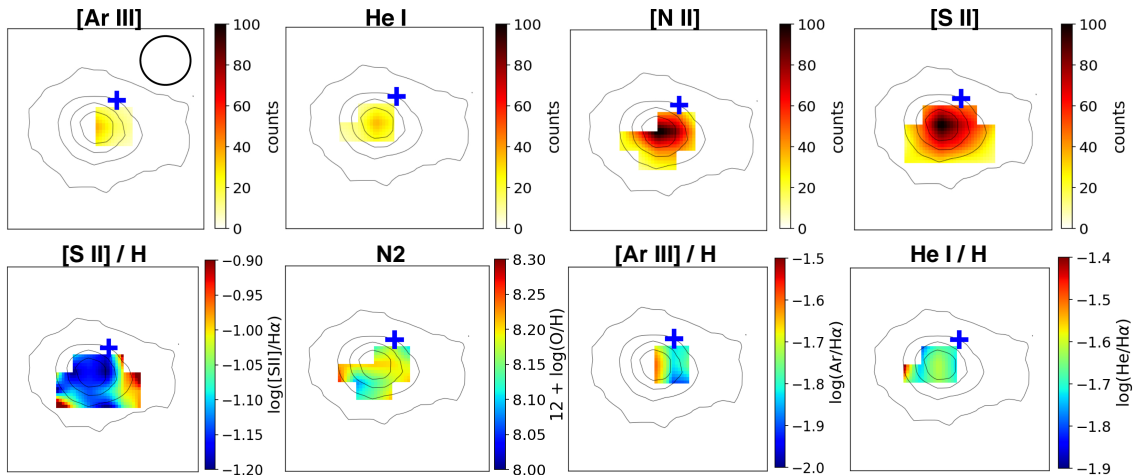


Fig. 6. Top: Line maps of transitions detected in the spectra of GRB 031203, the position of the GRB is indicated by a cross. Bottom (left to right): $[SII]/H\alpha$, metallicity using the N2 parameter, $[ArIII]/H\alpha$ and $HeI/H\alpha$. The circle in the σ plot shows its nominal resolution.

The metallicity in different spaxels varies between $12+\log(O/H)=7.9$ and 8.4 with a median of 8.2 with a mean error of 0.08 (full range between 0.01 and 0.2). These values have been derived from the original data, not the interpolated map shown in Fig. 6. The GRB site and the south-east have somewhat lower metallicities while the center is marginally more metal-rich. $[SII]/H\alpha$ follows a pattern similar to $[NII]/H\alpha$ but with the lowest values concentrated toward the center of the galaxy. High $[SII]/H\alpha$ ratios can give some indications of shocked regions. Fig. 7 shows the ratios of $[NII]/H\alpha$ and $[SII]/H\alpha$ for all spaxels where the four lines are detected with a $S/N>3$. Nearly all spaxels can be considered to be ionized by ionization from massive stars and not, for example, by shocks (Westmoquette et al. 2009a).

The galaxy shows an ordered velocity field and a possible disk component. The total line-of-sight velocity difference across the galaxy, however, is only $\Delta v = 53 \text{ km s}^{-1}$, which would point to a slowly rotating disk, a high inclination or a low mass, the latter of which is in conflict with the observations. The line width is rather uniform across the galaxy. However, there is a patch of low velocity width at the western end of the galaxy and a higher velocity region in the south, which we are going to investigate further in the following.

We extract integrated spectra of the GRB region, the high- and low- σ region and fit their line profiles (see Fig. 5). In all regions we clearly detect two components, a narrow, main peak with a σ of $\sim 35 \text{ km s}^{-1}$ and a weaker, broad component with a σ of $\sim 105 \text{ km s}^{-1}$, also detected in X-shooter (single slit) spectra

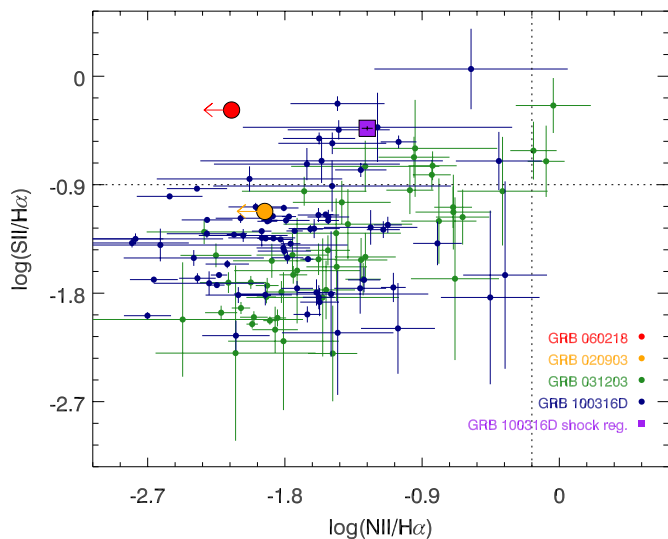


Fig. 7. Ratios of $[N II]/H\alpha$ and $[S II]/H\alpha$ for individual spaxels in the hosts of GRB 031203 and GRB 100316D as well as the integrated spectra of GRB 020903 and GRB 060218. The latter two only have upper limits for $[N II]/H\alpha$ since for $[N II]$ only an upper limit can be measured. Dashed lines indicate the ratios below which ionization can be considered as the main source for the line excitation (see e.g., Westmoquette et al. 2009a).

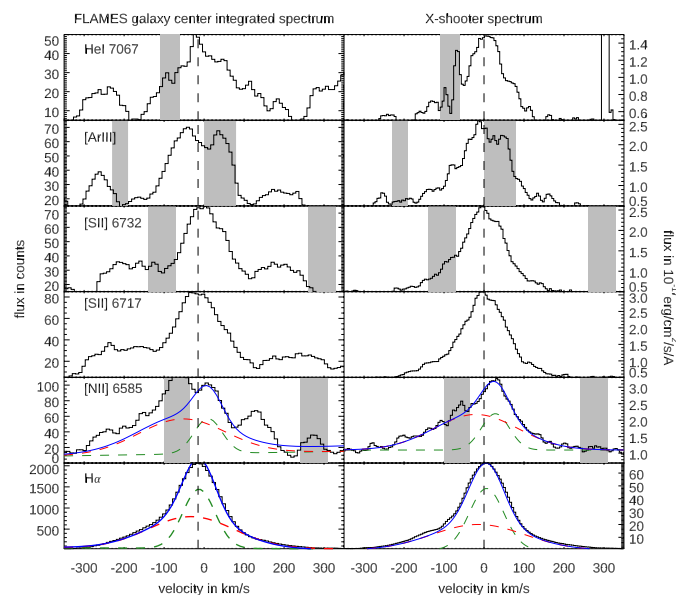


Fig. 8. GRB 031203: Comparison between weak emission line profiles in a spectrum integrating over the central 6×5 spaxels of the galaxy center (left column) and the same lines in an X-shooter spectrum presented in Guseva et al. (2011); Watson et al. (2011). The FLAMES spectra have been smoothed with a Gaussian kernel of 5 pixels in the spectral direction. Gray regions indicate contamination by residuals of atmospheric lines. For $[N II] \lambda 6585$ we fit a combination between a narrow and broad component based on the X-shooter spectrum using the same parameters to fit the line in the FLAMES spectrum.

of the host (Guseva et al. 2011; Watson et al. 2011). The relative strength of the component varies across the galaxy and explains the low- and high- σ regions in the line width map, which is derived from a single Gaussian fit to $H\alpha$. The broad component is strongest in the high- σ region in the South (“broad re-

gion”) and only slightly lower in the GRB region and weakest in the low- σ region in the Western part of the galaxy (“narrow region”). Across all the galaxy, the broad component is blueshifted compared to the main emission component. In contrast to GRB 030329, there are no afterglow spectra with absorption lines of this burst available to study a possible outflow in absorption.

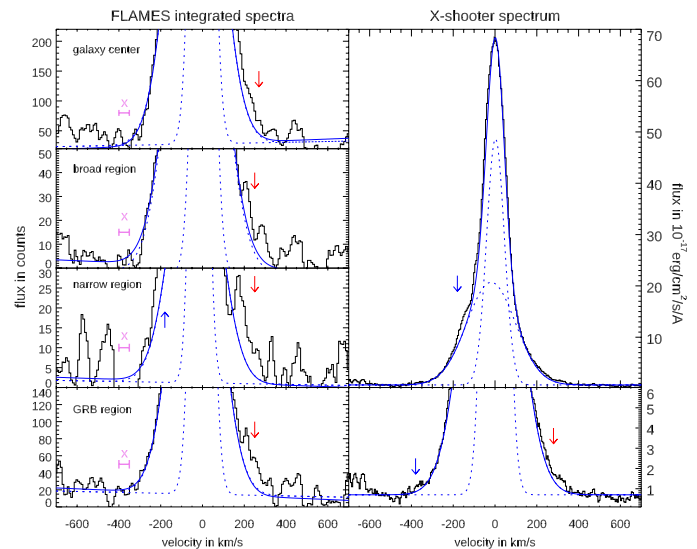


Fig. 9. GRB 031203: Zoom into $H\alpha$ to look for the high velocity excess emission in both red and blue wings claimed to be detected in the X-shooter spectra by Guseva et al. (2011). *Left:* Integrated regions in the FLAMES spectra explained in Fig. 5. *Right:* X-shooter spectrum. The scale for all panels (except the full size X-shooter panel) is ~ 0.1 of the $H\alpha$ peak value. Excess emission components that we detect in both spectra are marked with arrows with the same colors the same components detected in different spectra. The region where excess emission has been found in the blue wing of the X-shooter spectra but not in the FLAMES spectra is marked with a purple bar and cross. Zero velocity has been chosen as the centroid of the narrow emission component.

We also look for possible broad components in the other detected lines of $[Ar III]$, $He I$, $[S II]$ and $[N II]$ (in the following named “weak lines”). For this we made another integrated spectrum only comprising of the very central region of the galaxy (6×5 spaxels) not to be dominated by noise. In Fig. 8 we plot the lines in velocity space compared to $H\alpha$. All weak lines have an irregular profile due to the low S/N and, except for $[S II] \lambda 6717$, are affected by atmospheric lines. In the same figure we compare the lines to the ones from X-shooter data of the host presented in Guseva et al. (2011); Watson et al. (2011) (see Fig. 8). According to the finding chart in Guseva et al. (2011), the slit was oriented N-S with a width of 0.9–1.0 arcsec, covering a very similar region as the integrated spectra of the galaxy center. Despite the low S/N, all lines do show a broad wing that cannot be fit by a single Gaussian and excess emission on both sides and the emission stretches from ~ -150 to 150 km s^{-1} and possibly even up to 300 km s^{-1} in both red and blue.

Guseva et al. (2011) do not report a metallicity separately for the narrow and broad component, which they argue they are unable to provide due to the low S/N of the T_e sensitive $[O III] \lambda 4363$ line. Why they do not try to fit multiple components to $[N II] \lambda 6585$ is not mentioned. Although the $[N II]$ line is affected by an atmospheric line, we fit a double component similar to $H\alpha$ to the X-shooter spectra and use the same pa-

rameters to constrain the line in the FLAMES spectra of the galaxy center, which is more affected by the atmospheric line in the blue wing (see Fig. 8). Despite the atmospheric contamination, the broad component relative to the narrow component is stronger in [N II] than in H α . From the fits to the components in the X-shooter spectra we derive N2 metallicities of $12+\log(\text{O}/\text{H}) = 8.03 \pm 0.20$ for the narrow component and 8.19 ± 0.16 for the broad component. Although the metallicities are consistent within errors, there might be a small trend for a higher metallicity of the broad component.

Guseva et al. (2011) claim excess emission beyond the broad-narrow profile at $\sim -400 \text{ km s}^{-1}$ and $+350 \text{ km s}^{-1}$ in H α , H β and [O III]. In Fig. 9 we plot a zoom of H α in the three regions studied in Fig. 5 and the extraction of the central 5×4 spaxels (see last paragraph). We are not able to recover the excess emission at -400 km s^{-1} but we do see emission redward of the broad emission component at $200 - 300 \text{ km s}^{-1}$ in all regions, coincident with the excess emission in the X-shooter spectra (right panel). In some spectra this emission even looks like a narrow extra component in the red wing. Surprisingly, this component has the highest relative strength compared to the rest of the line in the “narrow region” with the lowest contribution of the broad component. In this region, we also clearly see an extra “shoulder” in the blue wing of H α at -150 to -200 km s^{-1} , also apparent in the X-shooter spectra plotted in Fig. 9 (right top panel in the figure) but not in the fit shown in Guseva et al. (2011), probably due to smoothing of the spectra. The reason for not detecting it in other regions might be that this extra component is blended with the broad component due to its higher line width in those regions.

3.4. GRB 050826

The host of GRB 050826 ($z = 0.297$) is visually a compact galaxy but has the highest stellar mass of the sample with $\log M^* = 9.79 M_\odot$. There is some discrepancy in the literature on the SFR inferred from different indicators: While Svensson et al. (2010) find a moderate SFR of $1.39 M_\odot/\text{yr}$ based on U-band photometry, Levesque et al. (2010b) derive a somewhat higher value of $2.9 M_\odot/\text{yr}$ from the H α emission line. Levesque et al. (2010b) determined a supersolar metallicity for the host galaxy based on the R_{23} parameter, taking the upper branch of the solution. Mirabal et al. (2007) detected also [O II] from the host and report the detection of the afterglow. No SN component has been detected due to the late confirmation of the afterglow. The initially reported transient (which later turned out to be the afterglow) was not coincident with the X-ray afterglow position (Halpern 2005), and not before Feb. 12, 2006 it was finally confirmed as the optical afterglow (Halpern & Mirabal 2006).

We only detect H α in the integrated spectrum of the galaxy. As this is the highest redshift host of the sample, despite its high mass and luminosity, the S/N of even H α is low. H α is also next to a bright atmospheric emission line in the very blue wing of the line, hence most of the profile is not affected. Given the stated high metallicity of the host by Levesque et al. (2010b), we should easily detect [N II]. However, our reanalysis resulted in a revised metallicity for this host (see Appendix B).

H α shows a double peak in part of the host (see the discussion below and Fig. 10). To be able to derive a velocity map fitting a single Gaussian, we first smooth the cube in wavelength with a Gaussian kernel of 7 pixels before fitting the resulting single peaked line. The velocity field of the galaxy is very non-uniform with no clear rotation and the difference in velocity across the galaxy is only 43 km s^{-1} . The width of the line has

a high σ of 73 km s^{-1} owing to the asymmetric and double line profile. The line width also shows some trend from lower velocities around 50 km s^{-1} on the N-W side, where the GRB is located, up to almost 100 km s^{-1} on the opposite side of the galaxy.

In Fig. 10 we fit H α to three different regions in the host and in the integrated spectrum of the entire galaxy. The H α line is broad at the center of the galaxy, asymmetric in the South dominated by the bluer component and clearly double-peaked in the northern part at the position of the GRB, which is also apparent in individual spaxels (hence it is not an artifact). This behavior explains the strange-looking velocity field, which is due to the shifting distribution of the double component across the host, similar to the host of GRB 020903.

We first fit the line with a double Gaussian component with a velocity difference of $\delta v = 60 \text{ km s}^{-1}$ and σ of $6-17 \text{ km s}^{-1}$ for both components. There is clear excess emission in both wings, hence we include a third, broad, component with a σ of 75 km s^{-1} . A fit to this component with a single Gaussian might not be optimal, alternatively, two narrower components could be fitted in the blue and red wings as we did for the host of GRB 030329. The centroid of the different components basically does not change, only their relative contributions. The broad component is present everywhere at a similar relative strength compared to the double narrow component. In the combined spectrum of the host, the broad component is less evident and the spectra could be equally well fit with a double component with a slightly higher σ than the narrow components in the triple component fit, underlining the importance of spatially resolved spectroscopy (see also Sect. 4.5).

3.5. GRB 060218

The host is the least luminous ($M_B = -15.9 \text{ mag}$, $\log M^* = 7.4 M_\odot$), smallest ($r_{80} = 0.55 \text{ kpc}$) and most metal poor host detected ($12+\log(\text{O}/\text{H}) = 7.6$ or $\sim 0.1 Z_\odot$, Wiersema et al. 2007; Kewley et al. 2007). Even HST imaging (Starling et al. 2012) does not resolve different HII regions. We detect only H α in the individual spaxels and marginally detect [S II] in the integrated spectrum of the host. The limit on the ratio of $\log([\text{N II}]/\text{H}\alpha) = -1.87$ from the integrated spectrum implies a metallicity limit of $12+\log(\text{O}/\text{H}) < 7.88$, consistent with the value determined in other longslit data.

The galaxy has no regular velocity field and does not show any sign of rotation. The dispersion is nearly constant, only at the S-W edge there might be a region with slightly higher width. The GRB lies in one of the regions with the lowest σ , just outside the brightest region of the galaxy. Since the galaxy is very compact and low-mass, the absence of a regular velocity field is not surprising.

Wiersema et al. (2007) obtained high-resolution UVES data at maximum light of the SN and find two kinematical components in NaD absorption separated by 24 km s^{-1} and a corresponding double component in [O III] emission (H α was out of the range). We tried to recover these two components in the H α line of the global spectra of the galaxy (see Fig. 4) and indeed the emission line does show a very small asymmetry. Fitting a single Gaussian does give a reasonable fit with only a small excess in the blue wing of H α . We then fit a double component with a velocity difference of $\delta v = 24.8 \text{ km s}^{-1}$ and σ of 12 and 15 km s^{-1} respectively. These values are similar to the ones found in Wiersema et al. (2007), who get a δv of 21.6 km s^{-1} and σ of 15 and 20 km s^{-1} , respectively. This double component initially gives a worse fit, but adding a small component in the blue wing with a σ of 8 km s^{-1} results in the best residuals.

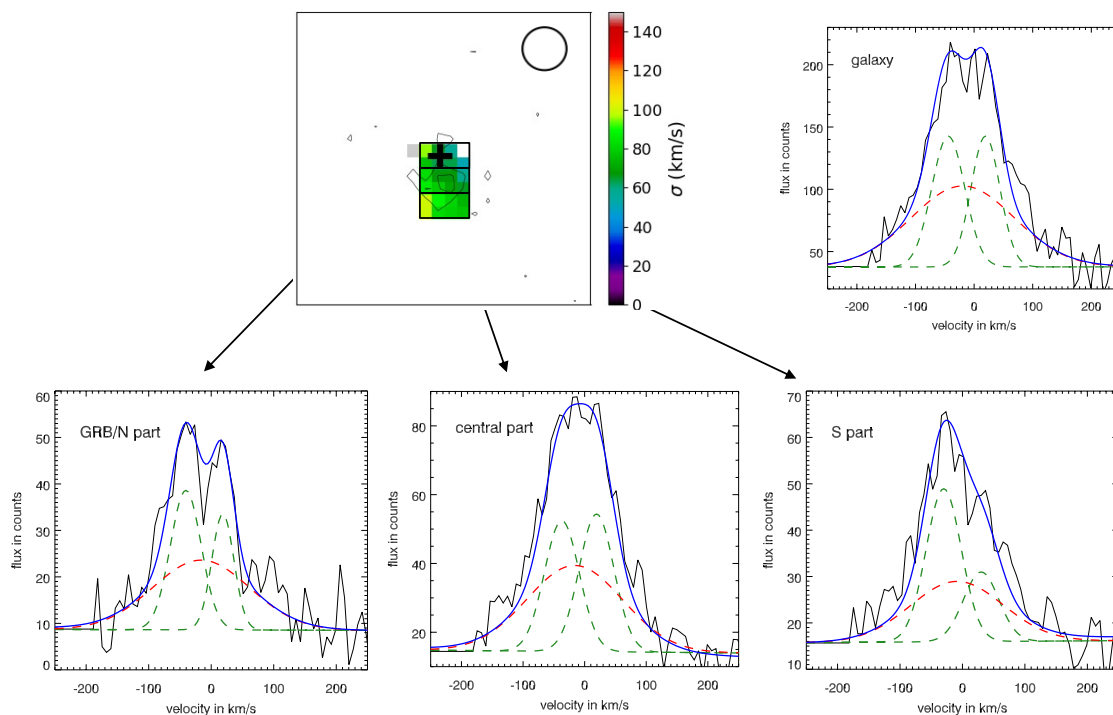


Fig. 10. GRB 050826: Fits to $H\alpha$ for three different regions in the host using a triple Gaussian component. We also show the profile and fit to the integrated spectrum of the host. The circle in the σ plot shows its nominal resolution.

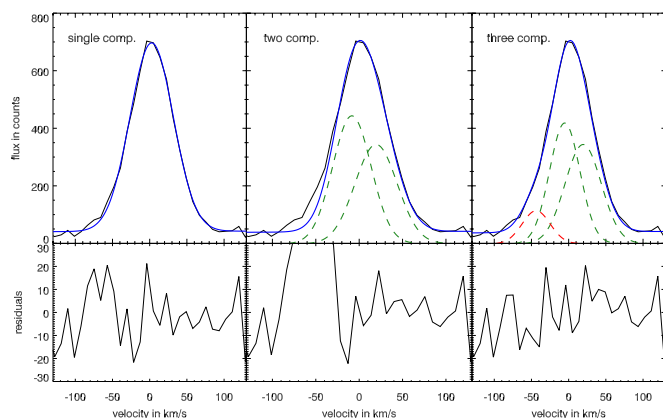


Fig. 11. $H\alpha$ fits and residuals for the host of GRB 060218. Left: Single Gaussian component, middle: two Gaussians with the same distance as the two components found in the afterglow spectra of GRB 060218 in Wiersema et al. (2007). Right: Additional component to fit the higher velocity emission in the blue wing of the emission line.

The presence of two main emission components would probably have been missed in our FLAMES spectra without the information from the UVES spectra. The absence of the third component in Wiersema et al. (2007) might have either been due to the higher continuum emission from the GRB-SN or its association with a part of the host not covered by the UVES spectra. While a single Gaussian profile has a similarly good fit as the triple profile, once fitting the double profile as in Wiersema et al. (2007), a third component is needed to account for the additional emission in the blue wing. Since our S/N is too low, we cannot extract spectra from different parts of the host to see whether this is associated with a specific region.

3.6. GRB 100316D

The host galaxy is a low-mass ($\log M = 8.93 M_{\odot}$), irregular, highly star-forming galaxy (Starling et al. 2012; Levesque et al. 2011) with several bright SF regions and its close distance allows for a detailed, resolved analysis (the angular size of the host is ~ 12 arcsec). The metallicity is low with $12 + \log(O/H) = 8.0 - 8.2$ (Levesque et al. 2011; Izzo et al. 2017) and it has total SFR of $1.2 M_{\odot}/\text{yr}$ (Izzo et al. 2017, henceforth I17). The GRB is located at the edge of the brightest and most extreme star-forming region in terms of SFR and metallicity.

The FOV of FLAMES only covers about half of the galaxy due to an error in the observational setup, but does include most of the bright SF regions in the northern part together with the GRB region. In individual spaxels we detect $H\alpha$, $[N II]$ and the $[S II]$ doublet at high S/N. I17 used the FLAMES data presented here for the kinematic analysis of the host. The MUSE data reveal a large number of emission lines including some not previously detected in GRB hosts such as $[N I]$ and $[Fe II]$. The detection of He I emission implies a very young stellar population and I17 derive an age of 5 Myr for the population at the GRB site.

The host of GRB 100316D is the only galaxy with sufficient S/N to make 2D maps of different emission components. $H\alpha$ shows a clear broad emission component in most of the spaxels. For spaxels with an $H\alpha$ line flux of > 80 counts we fit a double component using the PAN line fitting tool (see Fig. 13)¹. The broad component is strongest in the bright SF region next to the GRB region. The narrow component shows a regular velocity field of a rotating disk while the broad component is more chaotic. The velocity width of the narrow component is lowest at the center of the SF regions and higher on the edges while the width of the broad component is more erratic, which might be a simple effect of S/N.

¹ Developed by Rob Dimeo, <http://ifs.wikidot.com/pan>

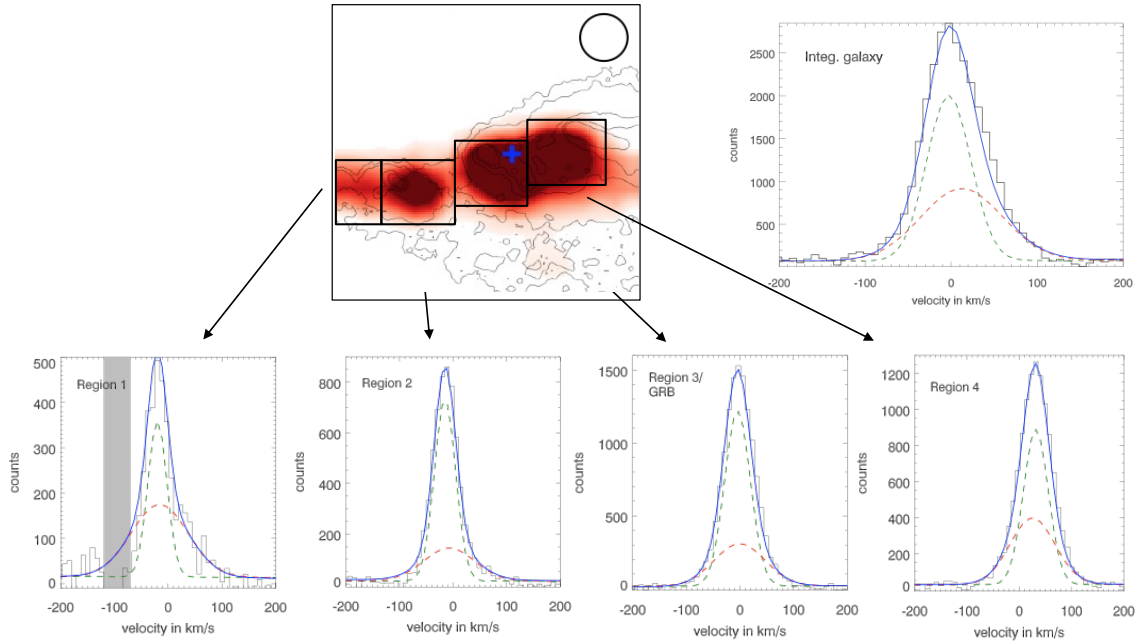


Fig. 12. GRB 100316D: Fits to $H\alpha$ in four integrated HII regions in the host and the integrated spectrum of all the spaxels in the FOV (which cover about 1/3 of the galaxy). The circle in the σ plot shows its nominal resolution.

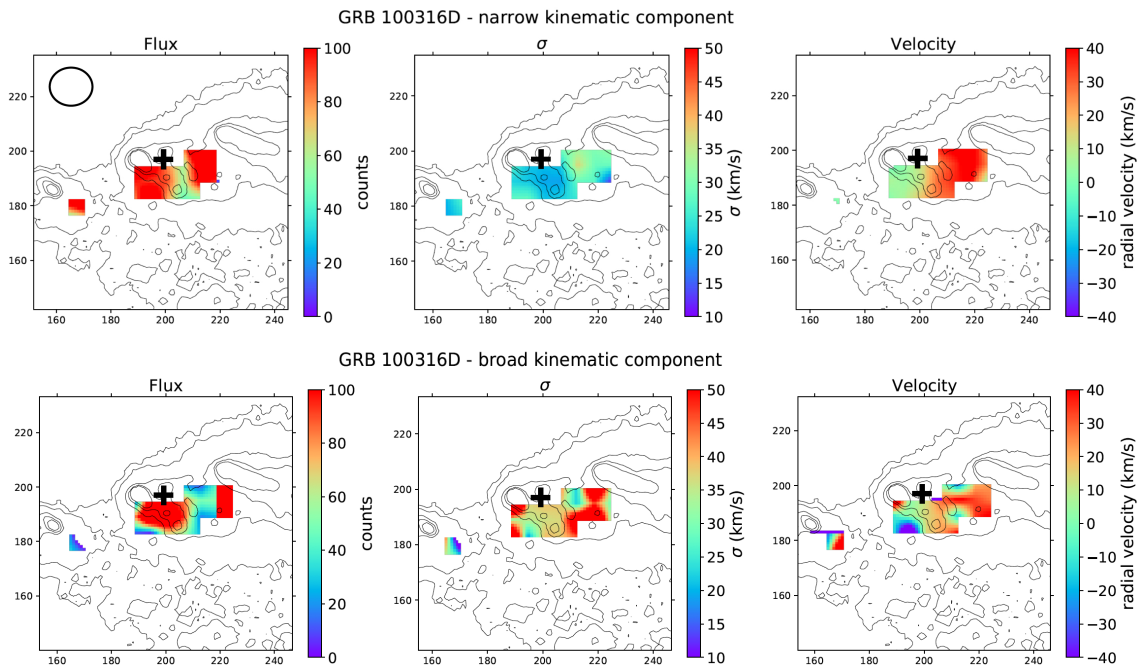


Fig. 13. GRB 100316D: Flux (in arbitrary units), velocity width and velocity field of the narrow (top) and broad (bottom) emission line components. The circle in the σ plot shows its nominal resolution.

In Fig. 12 we further study the integrated $H\alpha$ profile of four SF regions, but do not find any additional components. In individual regions, the broad component is blueshifted compared to the narrow component, however, in the integrated host spectrum, the profile is skewed to the red and the broad component appears redshifted compared to the main emission peak. This is an artifact from the combination of different regions with different

relative contributions and the velocity shift due to rotation of the galaxy.

I17 concluded from MUSE data that the GRB site is metal poor and next to the most extreme region in the host. The spatial resolution of the FLAMES data is slightly higher due to better seeing conditions ($\sim 0.8''$ for the FLAMES data vs. $\sim 1.1''$ for MUSE). The N2 metallicity follows the same pattern as in I17 with the lowest metallicity ($12 + \log(O/H) = 8.1$) in the bright SF

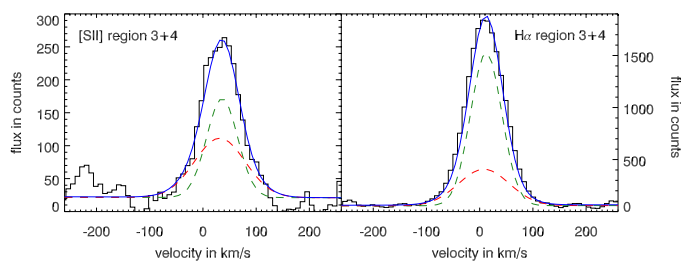


Fig. 14. GRB 100316D: Fit of a double component to [S II] λ 6717 in a region combining the SF region 3 (next to the GRB site) and SF region 4 and the corresponding fit to H α in the same regions.

region next to the GRB site. In the FLAMES data we also see a metal poor region with the same metallicity to the South-West of the GRB region. I17 only show a combined [S II+N II]/H α map, which is rather uniform in the part covered by the FLAMES data and higher values in a region they consider to be affected by shocks. Our [S II]/H α map shows no large variations but has particularly low values in the bright SF region next to the GRB site.

Also here we search for indications of shock excitation in the [S II]/H α vs. [N II]/H α plot (see Fig.7). Most spaxels are not affected by shock excitation. I17 found a region possibly affected by shocks in the Western part of the galaxy, outside the FOV of the FLAMES datacube. For comparison we plot the values found from an integrated spectrum of this possibly shocked region and the values are indeed indicative of shocks, however only in [S II]/H α , while the value for [N II]/H α is in a region that could be excited only by ionizing radiation.

We furthermore attempted to determine the metallicity of the broad and narrow component separately. Due to the low S/N of [N II] λ 6585 we use [S II] λ 6717. As we see in Fig. 14 the broad component is stronger compared to the narrow component than in H α . The fluxes of both components are very similar for [S II] while the narrow component of H α has a 2.5 times higher flux than the broad component. Deriving a concrete metallicity value is hindered by two problems: The S2 parameter requires both lines of the [S II] doublet since the ratio depends on the electron density which varies between ~ 1.5 and 0.5 for low and high densities, respectively. However, the $\lambda 6732$ line does not have enough S/N to fit both components. Second, the S2 metallicity has a weaker correlation with the N2 parameter. As we measure a ratio of ~ 1.5 for both the peak and the total flux ratio, we assume a low electron density and would therefore obtain metallicities of 8.3 ± 0.1 and 8.7 ± 0.2 for the narrow and broad component respectively, using the metallicity based on the S2 index from Yin et al. (2007).

4. Discussion

4.1. GRB host classification and velocity fields

Our sample of GRB hosts spans a wide range of stellar masses ($\log M^* = 7.5$ and $9.9 M_\odot$) and sizes ($r_{80} = 0.6$ to 12 kpc). In the following, we try to classify the galaxies using not only the mass, size and luminosity but also their velocity field.

BCDs show all kinds of velocity fields from ordered, disk-like rotation to highly disturbed velocity fields (see e.g. Östlin et al. 2001; Blasco-Herrera et al. 2013; Cairós et al. 2015; Cairós & González-Pérez 2017). Very compact dwarfs such as GPs (Lofthouse et al. 2017) often do not show a regular rotation field.

dIrrs are considered to be on the low-mass end of disk galaxies and have a regular velocity field with the only difference being the absence of a bulge component (e.g. Swaters et al. 2009).

A commonly used criterion to distinguish between dispersion vs. rotation dominated galaxies is the following: $v_{\text{shear}}/\sigma_0 > 1$ with $v_{\text{shear}} = 0.5 \Delta v$, where Δv is the difference between the minimum and maximum velocity of H α , and σ_0 the flux weighted average of the line width in all spaxels with S/N H α > 3 (see values in Tab. 2). Using σ_0 and v_{shear} we can derive a dynamical mass for the hosts. For spherical, relaxed systems the dynamical mass derived from the virial theorem is

$$M_{\text{dyn},\sigma} = \frac{4r_{50}\sigma^2}{G}$$

For rotation dominated systems the mass is derived as

$$M_{\text{dyn,rot}} = \frac{2v_{\text{rot}}^2 r_{50}}{G}$$

(Bellocchi et al. 2013) where $v_{\text{rot}} = 0.5 \Delta v$, identical to v_{shear} derived above. $M_{\text{dyn,rot}}$ technically comprises the mass within the half light diameter using the velocity at the half-light or effective radius while we use half the maximum velocity spread for v_{rot} . At the resolution of our dataset we can safely set $v_{\text{rot}} \sim v_{\text{eff}}$. In Tab. 2 we list the values from both methods, for any further calculations we use $M_{\text{dyn},\sigma}$ for the hosts of GRBs 030329, 060218, 020903 and 050826 and $M_{\text{dyn,rot}}$ for the hosts of GRBs 100316D and 031203. We do not apply any correction for inclination, which would affect the value of $M_{\text{dyn,rot}}$.

The two smallest hosts, those of GRB 030329 and GRB 060218, clearly fall in the category of BCDs. Both galaxies show almost no rotation and are dispersion dominated. The stellar masses are much lower than those from $M_{\text{dyn},\sigma}$, which could point to a more turbulent system. The contribution of the broad component is small and likely does not play a large role in determining σ_0 (see $F_{\text{broad}}/F_{\text{narrow}}$ in Tab. 3).

The hosts of GRB 020903 and GRB 100316D are dIrr with many different SF regions. The host of GRB 100316D has $r_{80} = 4$ kpc and shows intense SF around the GRB site but a low surface brightness in the rest of the galaxy. It also has the most pronounced disk-like rotation of our sample. I17 found that the galaxy is similar to other dIrr, being dominated by the disk rotation at small radii but by dark matter (DM) at larger radii. They concluded that the galaxy might not be completely virialized and suggested a close encounter with another (unknown) neighbor. This could explain the ongoing starburst in part of the galaxy ($\sim 40\%$ of the SF is located in the 25% of the galaxy covered by FLAMES). The host of GRB 020903 is compact, has no regular rotation curve, and is dominated by two main emission components close in velocity space that shift in strength across the galaxy. The host has $v_{\text{shear}}/\sigma_0 \sim 1$, note, however, that it is difficult to determine v_{shear} due to the double emission component.

Finally, the hosts of GRB 031203 and GRB 050826 are on the high mass end of dwarf galaxies. Watson et al. (2011) classified the host of GRB 031203 as a BCD due to its hard radiation field, high SF rate and absence of large amounts of dust. The host does show a clear rotation curve but a very low v_{max} of only ~ 25 km s $^{-1}$. $M_{\text{dyn},\sigma}$ and $M_{\text{dyn,rot}}$ match very well but are lower than the stellar mass. This could be due to a high inclination of the disk, however, the wind component is strong, which would speak for a relatively face-on system. With the lack of high resolution imaging it is difficult to determine its exact morphology. Formally, the host of GRB 050826 is dispersion dominated, but the two narrow components complicate the applicability of this

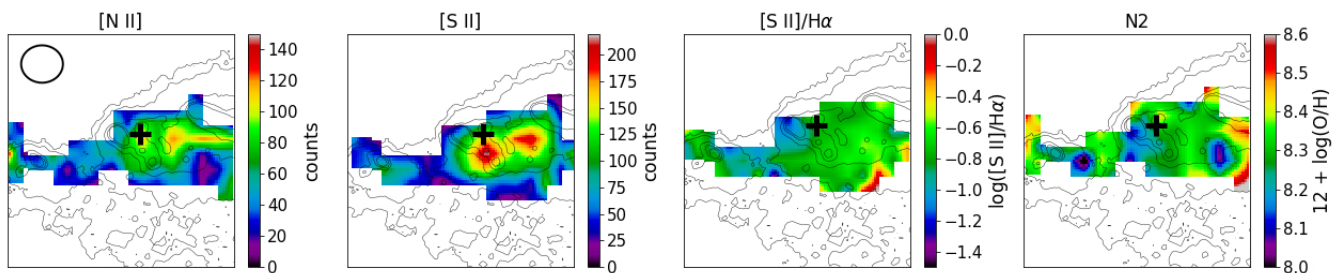


Fig. 15. Line maps of [N II] and the [S II] doublet in the spectra of GRB 100316D, [S II]/H α and metallicity using the N2 parameter (Marino et al. 2013). The circle in the σ plot shows its nominal resolution.

criterion. The double component and absence of a clear rotation field could be an indication for a merger. Also $M_{\text{dyn},\sigma}$ is much higher than $M_{\text{dyn,rot}}$ due to the “artificially” large σ from the double component. Again, the lack of high-resolution imaging prevents further conclusions.

4.2. GRB location

The location of the GRB is usually not at the region with the highest H α flux, but often close to it. Fruchter et al. (2006) and subsequent studies (e.g. Kelly et al. 2008; Svensson et al. 2010; Lyman et al. 2017) concluded from high spatial resolution HST imaging that GRB-SNe have a higher correlation with the brighter and bluer regions than any other SN type. In Tab. 1 we list the distance of the GRB from the brightest pixel in the H α map. Other studies take the brightest pixel in a broad-band filter (usually HST): Blanchard et al. (2016) use whatever filter available, while Lyman et al. (2017) only use the IR filter F160W, centered at 15,400 Å. Some of the filters used include H α at the corresponding redshift, but others probe only continuum emission.

The average distance from the brightest spaxel is 1.25 ± 0.93 kpc dominated by the large offset for GRB 050826, removing this host we get an average of 0.88 ± 0.26 kpc. These values are well in agreement with distances reported in the literature: 1.4 ± 0.8 kpc (Bloom et al. 2002), 1.2 ± 0.2 kpc (Blanchard et al. 2016) and 1.0 ± 0.2 kpc (Lyman et al. 2017). Normalizing the distance from the brightest H α spaxel to the galaxy r_{80} gives an average normalized distance of 0.66 ± 0.37 . Lyman et al. (2017) found an average d_{GRB}/r_{80} of only 0.3 (comprising hosts up to $z = 2.7$), while a recent work comparing GRB and BL-Ic SN hosts without GRBs (Japelj et al. 2018) found $d_{\text{GRB}}/r_{50} = 0.98$ for GRB hosts (which partly comprises the sample presented here). The GRB location is also always inside the 80% light radius of the host (see Tab. 1). To test the hypothesis of a correlation between the SFR and the GRB location, we perform a Monte Carlo simulation, scaling the probability of a GRB being produced in a specific location with the H α flux. From this we obtain an expected average distance from the brightest pixel to the GRB location of 2.5 ± 1.5 kpc, which is larger than the distances that we measured. This indicates that GRBs do not occur in any random SF region, but are rather associated with massive, bright SF regions capable of producing the required massive progenitors.

Hammer et al. (2006) proposed that GRBs might be runaway stars from extreme HII regions. GRB 980425 is 800 pc from a bright region with WR lines, however, the GRB site itself is a smaller SF region (Fynbo et al. 2000). For GRB 020903, Hammer et al. (2006) found a distance of 450 pc from the brightest pixel of the SF region we named “GRB region”. However, while

none of the GRB sites are associated with the brightest HII region, they are always associated with some SF region. This could imply that a luminous SF region with a large number of massive stars is not the only determining factor or that GRB progenitors are not necessarily the most massive stars.

The GRB is usually located in a region of the galaxy with low line width (see Fig. 1). This is a common pattern in dwarf galaxies, where larger σ values are found in between HII regions (see e.g. Cairós & González-Pérez 2017, and references therein). In the three hosts where we resolve a broad component in different regions, the GRB region does clearly show an underlying broad component but it is usually not the region with the highest relative luminosity of the broad component. For the host of GRB 031203, the absolute flux of the broad component is highest in the GRB region, but the relative contribution is larger in the “broad region”. In some cases, geometric effects might play a role in determining the actual observed strength of the broad component.

4.3. The broad emission component and evidences for a star-burst wind

All galaxies in our sample show an underlying broad component or high velocity emission. For GRB 030329 and GRB 050826 two separate components might be present in the blue and red wings (see Figs. 4 and 10). Similar looking excess emission in H α has been observed in a sample of nearby extremely metal poor (XMP) dwarfs (Olmo-García et al. 2017) and explained with expanding shells that can be more or less symmetric and/or affected by differential dust extinction. Three galaxies of our sample also have multiple narrow components. Even galaxies that appear compact, however, can have multiple components in velocity due to the orientation of the galaxy, see e.g. the host of GRB 100418A (de Ugarte Postigo et al. 2018).

The narrow and broad components are kinematically detached. While the narrow component follows the general velocity field the velocity of the broad component stays almost constant. The broad component is blueshifted, concentrated in the most intense SF region and more metal-rich. These results strongly hint to an outflow causing these components, since an inflow should have lower metallicity containing more pristine gas from the IGM.

The possibly best example for an outflow is the host of GRB 031203, where the emission spans 300–400 km s $^{-1}$ with possible additional components up to 700 km s $^{-1}$. This goes beyond the normal rotation field of a galaxy of this mass of ~ 150 km s $^{-1}$. The broad component is blue-shifted and likely more metal-rich, adding to the outflow hypothesis. The broad component is strongest in the central parts and weaker in the Western

“tail”, implying that it might originate from the brightest SFR and is either blocked in some parts or not spherically symmetric. The excess emission in the red wing is stronger in the Western part but visible throughout the host. This might be an additional outflow component or shell or it could be connected to the radio emission from HI detected in Michałowski et al. (2015), claimed to be infalling, metal poor gas.

For two hosts (GRB 060218 and GRB 030329) we can compare emission line kinematics from warm gas with absorption line kinematics from cold gas (Wiersema et al. 2007; Thöne et al. 2007). The absorption in GRB 030329 clearly supersedes the velocities from pure rotation, while for GRB 060218 the absorption lines of NaD match the components of the emitting gas. The two galaxies are similar in size and metallicity and both probably consist of a single large star-forming region. Galactic winds have been regularly detected also in NaD absorption (see e.g. Martin 2006; Veilleux et al. 2005), however, note that NaD has a different ionization energy than Mg I and II. One explanation could be that the outflow cones have small opening angles, hence for GRB 030329 the wind would point toward us while for GRB 060218 we see the galaxy outside of the wind cone. The fact that the host of GRB 030329 has hardly any velocity field while for GRB 060218 we do observe some rotation could point to a different inclination of these two galaxies.

M82 shows a very similar narrow-broad profile, which can be traced out to large distances, and some regions at the base of the wind have double components associated with expanding shells (Westmoquette et al. 2009b,a). BCDs frequently show broad components, e.g. Haro 14 (Cairós & González-Pérez 2017), Haro 11 (Östlin et al. 2015), NGC 4449 (Kumari et al. 2017), UM448 (James et al. 2013), Mrk996 (James et al. 2009) or NGC 1569 (Westmoquette et al. 2007). Westmoquette et al. (2007) conclude that the broad component in the center of NGC 1569 originates from the interaction between a strong stellar wind and cold gas knots, producing a turbulent mixing layer on the surface which powers the observed starburst wind. Haro 11 (Östlin et al. 2015) shows a triple component in [S III], one with $\sigma \sim 90 \text{ km s}^{-1}$, but this component follows the stellar velocity field and might be a superposition of several unresolved lines. Outflows in absorption have been detected for the majority of starburst galaxies with fractions ranging from 75% (Chisholm et al. 2015) to 90% for face-on galaxies (Heckman et al. 2015). Outflows in both absorption and emission have been detected in NGC 7552 (Wood et al. 2015), a face-on spiral galaxy, showing blue-shifted emission components (σ up to 300 km s^{-1}) and blue-shifted absorption components up to 1000 km s^{-1} .

At higher redshifts Amorín et al. (2012) find broad components in six GP galaxies at $z = 0.1 - 0.3$ but with higher width than in our sample (σ of $50-110 \text{ km s}^{-1}$, full width zero intensities $>650 \text{ km s}^{-1}$). They associate these components with stellar winds or supernova remnants and exclude turbulent mixing layers since they would only be observed in the Balmer lines but not the forbidden lines as it is also the case in our FLAMES sample. IFU spectra of $z \sim 0.2$ GPs (Lofthouse et al. 2017) show evidence for a broad component with $\sigma > 85 \text{ km s}^{-1}$. The extreme starburst in GPs together with a large number of WR stars could explain the larger velocities observed. GPs also show outflows in absorption and many are Lyman- α emitters, possible analogs to high redshift galaxies responsible for the escape of Ly α photons (see e.g. Henry et al. 2015; Yang et al. 2017). Broad-narrow line profiles have been detected in massive star-forming galaxies at $z \sim 2$ in the SINS survey (Genzel et al. 2011; Newman et al. 2012; Davies et al. 2019). The blue-shifted broad profiles are associated with the brightest regions/clusters attributed to power-

ful winds in which the outflow rate can even supersede the SFR, quenching their own SF rather efficiently.

Winds could also explain abundances differences in BDCs. In NGC 4449, the central SF region is more metal poor than the outskirts of the galaxy, something also observed in other dwarf starbursts (Sánchez Almeida et al. 2015; Elmegreen et al. 2016). Kumari et al. (2017) propose an outflow of metal-rich gas acting stronger in the region with the highest SFR than in the outskirts, but also the inflow of metal-poor gas or pre-enriched gas giving rise to new SF regions after a merger are viable explanations. James et al. (2009) found a large enhancement of N/O and nitrogen abundance in Mrk996 in the broad emission component while the narrow component shows a normal N/O ratio. However, in UM448, WR features (albeit rather faint) are associated with a region showing a weaker broad component but an enhancement in N/H and N/O (James et al. 2013). The authors speculate that WR stars alone cannot be responsible for the N/O enhancement and suggest an inflow of metal-poor gas leading to a decrease of the O abundance. Clearly, different galaxies are influenced by a varying interplay between in- and outflows, which are hard to study beyond the local Universe.

4.4. Correlations between components and galaxy properties

We searched for possible correlations between the broad components and the properties of the host (stellar mass, luminosity, metallicity and SFR, see Tabs. 1, 2, and 3 and Fig. 16). As an additional value we derived the maximum outflow velocity of the gas defined as

$$V_{\text{max}} = |\Delta v(\text{broad} - \text{narrow}) - 0.5 \text{FWHM}_{\text{broad}}|$$

and listed in Tab. 3 (Arribas et al. 2014; Veilleux et al. 2005). For the hosts of GRBs 020903, 050826 and 060218 we use Δv between the bluest narrow and the broad component, for the host of GRB 030329 we use the blue shifted additional component. Note that in this section we use FWHM instead of σ .

We only find correlations between the SFR and the broad component, namely with 1) the FWHM of the broad component (panel A), 2) the flux ratio between broad and narrow component(s) (panel B) and 3) the maximum velocity V_{max} (panel C). The only outlier from correlation 3) is GRB 020903 where the position of the broad component relative to the bluer narrow component shifts between negative and positive velocities. The Pearson’s coefficient for all those correlations is good with values of 0.94, 0.96 and 0.94, while the (non) correlation between the FWHM and ΣSFR or the stellar mass yield coefficients of <0.7 . Hosts with broader components, higher relative flux of the broad component, and higher V_{max} have also higher SFRs (see Fig. 16). In the host with the highest SFR, GRB 031203, the flux of the broad component is higher than the one in the narrow component by a factor of 1.5, hence the contribution of the outflowing material is considerable compared to the emission from the bulk of the gas in the galaxy. We note that our sample might be too small to establish firm correlations, however, it is the largest currently available sample of GRB hosts which allows to search for those correlations.

We do not find a correlation between $\log M^*$ and the width of the broad component (panel E) but there is some correlation between the FWHM fitting a single Gaussian and $\log M^*$ (values listed in Tab. 2 as σ_{int}) with a Pearson’s coefficient of 0.88 (panel F). The latter confirms the widely established “stellar mass Tully-Fisher” (sTF) $M^*-\sigma$ relation (see e.g. Miller et al.

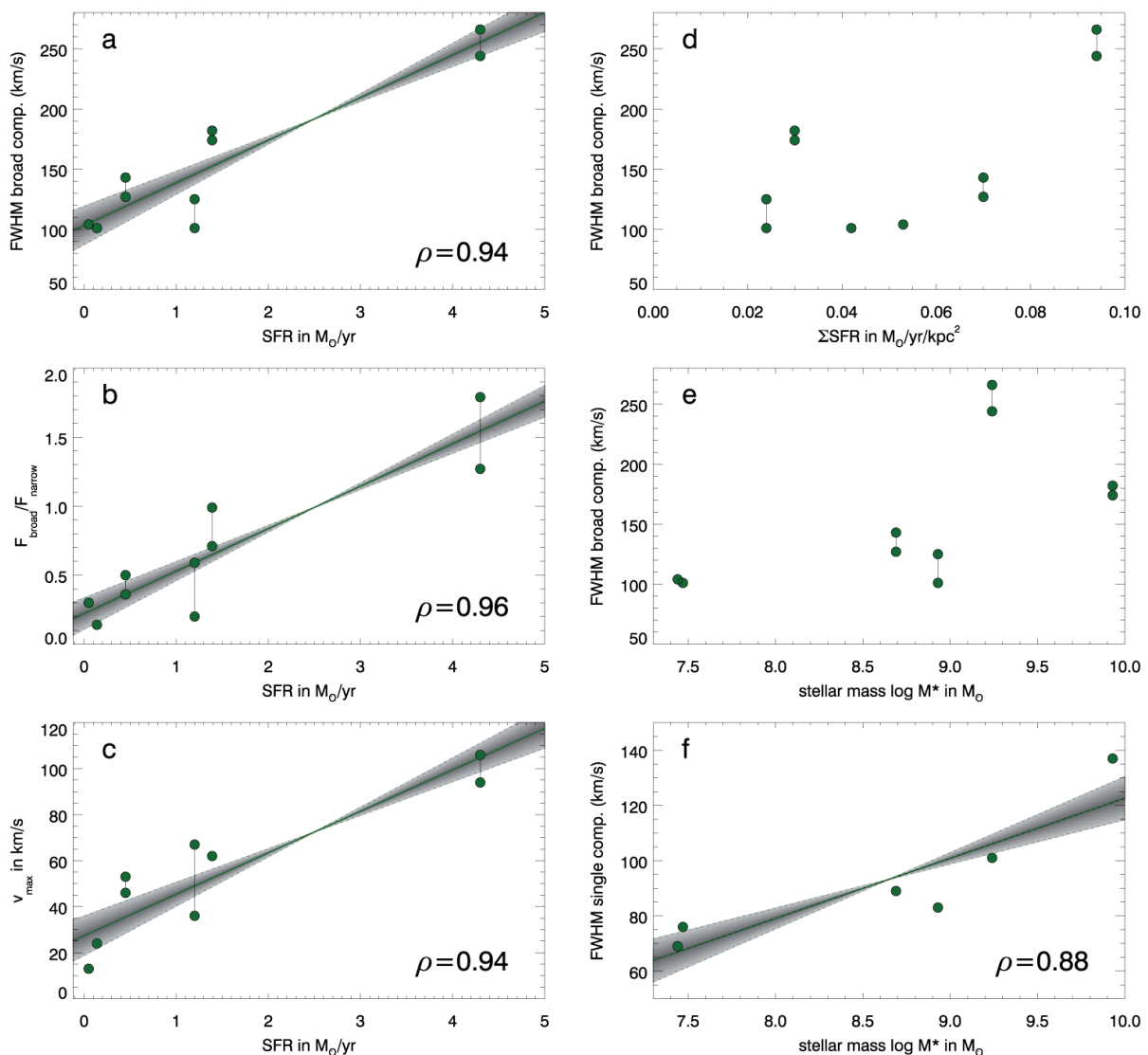


Fig. 16. Panel A, B & C: Correlations between SFR and FWHM of the broad emission component, $F_{\text{broad}}/F_{\text{narrow}}$ and V_{max} (see Sect. 4.4). For hosts with a range of values we plot the upper and lower limits. In panels with linear correlations, green lines are the linear fit, the shaded area is the error of the slope. In case of a range of values for the y-axis we take the average to fit the correlation. Panel D&E: FWHM of the broad component vs. SFR density and M^* for which there are no clear correlations. Panel F: A weak correlation is also found for M^* and the width of a single Gaussian fit to the integrated galaxy spectra (σ_{int} in Tab. 2, here plotted as FWHM for consistency with the other plots), which corresponds to a stellar mass Tully Fisher relation. ρ indicates the Pearson’s coefficient for the different correlations.

2012). The fact that the narrow component correlates with M^* , but the broad component does not, confirms that the broad component is not related to the velocity field of the galaxy, as we have specifically shown for GRB 100316D (see Fig. 13).

Several studies have tried to establish scaling relations between winds traced by absorption lines and SFR or stellar mass. They usually find the SFR, ΣSFR or SFR/M^* to correlate with the outflow velocity (measured as σ or V_{max}) but with different slopes (see e.g. Erb et al. 2012; Arribas et al. 2014; Chisholm et al. 2015; Heckman & Borthakur 2016, and references therein), but not the absolute SFR as it is the case for GRB hosts. Heckman (2003) suggests that there is a minimum ΣSFR density of $\sim 0.1 M_{\odot}/\text{y}/\text{kpc}^2$ needed to launch an outflow from a rotating disk, higher than the SFR densities observed in the FLAMES sample. Since the SFR density depends on the inclination angle, an incorrect inclination could change the value slightly. Extinction is not an issue as this would affect both ΣSFR and SFR.

Tanner et al. (2017) model a starburst wind and produce synthetic absorption lines. They only find a correlation with SFR and ΣSFR below a certain threshold, however the observed velocities can be much lower than the actual wind velocity. This also explains different slopes using absorption lines, since they trace SFRs above and below the threshold as well as different ions. Maseda et al. (2014) do not find a correlation between M^* and σ (as measured from a single Gaussian fit) in a sample of extreme emission line galaxies (EELGs) at $z = 1-2$, however, their mass range is rather small. Those galaxies have a σ around 50 km s^{-1} with some reaching up to 200 km s^{-1} but they do not detect a broad component like Amorín et al. (2012) for GPs (which are simply EELGs at a certain redshift). Maseda et al. (2014) conclude that the gas fraction must be higher for those galaxies in order to be stable, and part of the gas rapidly turns into stars before the starburst shuts down again. This process might be supported by winds or outflows.

Comparing the FLAMES sample to a large sample using MANGA data (Rodríguez del Pino et al. 2019), our galaxies have much higher relative strengths of the broad vs. narrow component but lower outflow speeds V_{\max} and σ of the broad component. Also, at the low masses of our sample galaxies, the detection rate of outflows should be rather low and not 100% (Rodríguez del Pino et al. 2019). We note, however, that the sample selection is different from the GRB hosts presented here, which might explain the differences. On the other hand, the low masses make it likely for the material to actually escape the galaxy. Using the dynamical mass of the galaxies derived in Sect. 4.1 (see Tab. 2), we can derive the escape velocity for gas at $r=r_{80}$:

$$v_{\text{esc}} = \sqrt{\frac{2M_{\text{dyn}} G (1 + \ln(r_{\text{max}}/r))}{3r}}$$

taking a ratio of $r_{\text{max}}/r = 10$ where r_{max} is the maximum radius of an isothermal gravitational potential (Arribas et al. 2014). For the hosts of GRB 031203 and GRB 100316D the outflowing gas might be able to escape the galaxy, for GRB 031203 V_{\max} even superseeds V_{esc} by a factor of 2. The gas in the highest mass host, GRB 050826, does not reach escape velocity and, surprisingly, neither in the smallest host, GRB 060218. Rodríguez del Pino et al. (2019) and Arribas et al. (2014) concluded that beyond log $M \sim 10.4$, it is rare that the gas reaches escape velocity.

4.5. The perils of low spatial resolution

Our study shows the complications of kinematic studies with poorly resolved and/or longslit data. Integrated spectra usually show less components than the spectra of individual HII regions. For the host of GRB 100316D the integrated spectrum even displays an erroneous position of the broad component. The main problem is the fact that the broad component is almost constant in velocity, while the narrow component follows the rotation field. Moiseev & Lozinskaya (2012) analyzed the effect of decreasing resolution on IFU data in nearby starbursts. High flux values get smoothed out and the range of extreme σ values decreases, however, the median σ value remains constant. Regions with high σ at the edge of HII regions blend together to larger structures of seemingly high σ .

One has to be especially careful with longslit data. If the slit is oriented along the velocity field, collapsing it to a single 1D spectrum can get broad components to be lost in the broadening of the narrow component due to the velocity shift. If the orientation of the galaxy is not known, it might lead to wrong conclusions on the presence/absence of different kinematic components. Another difficult case is hosts with double or multiple narrow components. Since the individual subcomponents can follow their own velocity fields, blending them together with the velocity change can mimic a velocity field of a normal rotating disk. However, this should be relatively easy to distinguish from the velocity field of a rotating disk.

5. Conclusions

This paper presents the first spatially resolved data of low-redshift long duration GRB hosts at high spectral resolution, able to distinguish different kinematical components. We study the kinematics using $H\alpha$ and include a limited study on abundances:

- Low redshift GRB hosts are often BCDs and dIrrs with properties similar to the general population of these galaxies.

- Only two out of six hosts show a rotating disk. The two most compact hosts are dispersion dominated with very little rotation. The remaining two have a double narrow component which could point to systems in the process of merging.
- The GRB is close to but not at the brightest region nor that with the highest σ . This might be an indication for kicks from a binary companion or some particular conditions in the SF region that give rise to the GRBs.
- All galaxies have underlying broad components with a σ of $50 - 110 \text{ km s}^{-1}$ blueshifted compared to the main emission peak. We interpret these components as outflows due to winds from young stars and/or supernova explosions. For low mass hosts, the velocities of the wind (V_{\max}) supersede escape velocity and the gas might actually be capable of leaving the galaxy.
- For GRB 030329, there is evidence for a metal-rich outflow from absorption lines, but GRB 060218, a very similar galaxy, does not show absorption lines at high velocities. Unfortunately, at low redshift we often lack absorption line spectra, while at high- z those absorption components stretching over several 100 km s^{-1} are detected frequently.
- The strength of the broad component changes across the galaxy but the largest contribution or width is not necessarily associated with the region of highest SFR. The velocity field of the broad component does not follow the general rotation field of the galaxy.
- The broad component seems to be more metal-rich, another indication for an outflow transporting enriched gas away from the galaxy via winds or SN explosions.
- We find a correlation between the SFR of a host and 1) the width of the broad component, 2) the relative strength compared to the narrow component and 3) the maximum gas velocity V_{\max} , but no correlation with the stellar mass or the SFR density, the latter of which is usually correlated to the wind component in SF galaxies. In GRB hosts the broad component seems to be correlated with the total amount of current SF in the host.
- Detailed kinematics crucially depend on spectral and spatial resolution. Integration over too large regions can result in erroneous line profiles, especially if the integration is done across the velocity field or.

A larger sample with higher S/N and spectral resolution would be very much desired, but is difficult with current instrumentation. It would also be interesting to compare GRB hosts with those of SLSNe, which show even lower metallicities and higher SF rates (see e.g. Leloudas et al. 2015; Schulze et al. 2018). A unique feature of GRBs is that, within a certain redshift range, we are able to probe both emission and absorption line kinematics, something which is very expensive to do e.g. for quasar intervening systems. The study of GRB host kinematics is still in its infancy, particularly in 3D, but can give us important indications on the processes of SF in starburst galaxies.

Acknowledgements. CT and AdUP acknowledge support from AYA2017-89384-P, CT and AdUP also from a Ramón y Cajal fellowships RyC-2012-09984 and RyC-2012-09975, LI from a Juan de la Cierva Integración fellowship IJCI-2016-30940. DAK acknowledges support from the Spanish National Research Project RTI2018-098104-J-I00 (GRBPhot). JFAF acknowledges support from the Spanish Ministerio de Ciencia, Innovación y Universidades through the grant PRE2018-086507. SDV acknowledges support from the French National Research Agency (ANR) under contract ANR-16-CE31-0003. LC is supported by YDUN grant DFF 4090-00079. Ground based observations were collected at the VLT under program 092.D-0389(A).

References

- Amorín, R., Vílchez, J. M., Hägele, G. F., et al. 2012, *ApJ*, 754, L22
- Arribas, S., Colina, L., Bellocchi, E., Maiolino, R., & Villar-Martín, M. 2014, *A&A*, 568, A14
- Ashley, T., Simpson, C. E., & Elmegreen, B. G. 2013, *AJ*, 146, 42
- Ashley, T., Simpson, C. E., Elmegreen, B. G., Johnson, M., & Pokhrel, N. R. 2017, *AJ*, 153, 132
- Bekki, K. 2008, *MNRAS*, 388, L10
- Bellocchi, E., Arribas, S., Colina, L., & Miralles-Caballero, D. 2013, *A&A*, 557, A59
- Bersier, D., Fruchter, A. S., Strolger, L.-G., et al. 2006, *ApJ*, 643, 284
- Blanchard, P. K., Berger, E., & Fong, W.-F. 2016, *ApJ*, 817, 144
- Blasco-Herrera, J., Fathi, K., Östlin, G., Font, J., & Beckman, J. E. 2013, *MNRAS*, 435, 1958
- Bloom, J. S., Kulkarni, S. R., & Djorgovski, S. G. 2002, *AJ*, 123, 1111
- Boquien, M., Burgarella, D., Roehly, Y., et al. 2019, *A&A*, 622, A103
- Bruzual, G. & Charlot, S. 2003, *MNRAS*, 344, 1000
- Bufano, F., Pian, E., Sollerman, J., et al. 2012, *ApJ*, 753, 67
- Burgarella, D., Buat, V., & Iglesias-Páramo, J. 2005, *MNRAS*, 360, 1413
- Cairós, L. M., Caon, N., & Weibacher, P. M. 2015, *A&A*, 577, A21
- Cairós, L. M. & González-Pérez, J. N. 2017, *A&A*, 608, A119
- Calzetti, D., Armus, L., Bohlin, R. C., et al. 2000, *ApJ*, 533, 682
- Campana, S., Mangano, V., Blustin, A. J., et al. 2006, *Nature*, 442, 1008
- Cano, Z., Bersier, D., Guidorzi, C., et al. 2011a, *ApJ*, 740, 41
- Cano, Z., Bersier, D., Guidorzi, C., et al. 2011b, *MNRAS*, 413, 669
- Cano, Z., Wang, S.-Q., Dai, Z.-G., & Wu, X.-F. 2017, *Advances in Astronomy*, 2017, 8929054
- Cardamone, C., Schawinski, K., Sarzi, M., et al. 2009, *MNRAS*, 399, 1191
- Cardelli, J. A., Clayton, G. C., & Mathis, J. S. 1989, *ApJ*, 345, 245
- Chabrier, G. 2003, *PASP*, 115, 763
- Chen, H.-W. 2012, *MNRAS*, 419, 3039
- Chisholm, J., Tremonti, C., & Leitherer, C. 2018, *MNRAS*, 481, 1690
- Chisholm, J., Tremonti, C. A., Leitherer, C., et al. 2015, *ApJ*, 811, 149
- Chornock, R., Berger, E., Levesque, E. M., et al. 2010, *arXiv e-prints*, arXiv:1004.2262
- Christensen, L., Vreeswijk, P. M., Sollerman, J., et al. 2008, *A&A*, 490, 45
- Ciesla, L., Charmandaris, V., Georgakakis, A., et al. 2015, *A&A*, 576, A10
- Cobb, B. E., Baily, C. D., van Dokkum, P. G., Buxton, M. M., & Bloom, J. S. 2004, *ApJ*, 608, L93
- Cobb, B. E., Baily, C. D., van Dokkum, P. G., & Natarajan, P. 2006, *ApJ*, 645, L113
- Coward, D. M., Howell, E. J., Branchesi, M., et al. 2013, *MNRAS*, 432, 2141
- Dale, D. A. & Helou, G. 2002, *The Astrophysical Journal*, 576, 159
- Dale, D. A., Helou, G., Magdis, G. E., et al. 2014, *ApJ*, 784, 83
- Davies, R. L., Förster Schreiber, N. M., Übler, H., et al. 2019, *ApJ*, 873, 122
- de Ugarte Postigo, A., Thöne, C. C., Bensch, K., et al. 2018, *A&A*, 620, A190
- Dimeo, R. 2005, available at <http://www.ncnr.nist.gov/staff/dimeo/panweb/pan.html>
- Elmegreen, B. G. & Hunter, D. A. 2015, *ApJ*, 805, 145
- Elmegreen, D. M., Elmegreen, B. G., Sánchez Almeida, J., et al. 2016, *ApJ*, 825, 145
- Erb, D. K., Quider, A. M., Henry, A. L., & Martin, C. L. 2012, *ApJ*, 759, 26
- Ferrero, P., Kann, D. A., Zeh, A., et al. 2006, *A&A*, 457, 857
- Flores, H., Hammer, F., Puech, M., Amram, P., & Balkowski, C. 2006, *A&A*, 455, 107
- Fruchter, A. S., Levan, A. J., Strolger, L., et al. 2006, *Nature*, 441, 463
- Fynbo, J. U., Holland, S., Andersen, M. I., et al. 2000, *ApJ*, 542, L89
- Gal-Yam, A., Moon, D. S., Fox, D. B., et al. 2004, *ApJ*, 609, L59
- Genzel, R., Newman, S., Jones, T., et al. 2011, *ApJ*, 733, 101
- Gorosabel, J., Larionov, V., Castro-Tirado, A. J., et al. 2006, *A&A*, 459, L33
- Gorosabel, J., Pérez-Ramírez, D., Sollerman, J., et al. 2005, *A&A*, 444, 711
- Guseva, N. G., Izotov, Y. I., Fricke, K. J., & Henkel, C. 2011, *A&A*, 534, A84
- Halpern, J. P. 2005, *GRB Coordinates Network*, 3891
- Halpern, J. P. & Mirabal, N. 2006, *GRB Coordinates Network*, 5982
- Hammer, F., Flores, H., Schaerer, D., et al. 2006, *A&A*, 454, 103
- Han, X. H., Hammer, F., Liang, Y. C., et al. 2010, *A&A*, 514, A24
- Heckman, T. M. 2003, in *Revista Mexicana de Astronomía y Astrofísica*, vol. 27, Vol. 17, *Revista Mexicana de Astronomía y Astrofísica Conference Series*, ed. V. Avila-Reese, C. Firmani, C. S. Frenk, & C. Allen, 47–55
- Heckman, T. M., Alexandroff, R. M., Borthakur, S., Overzier, R., & Leitherer, C. 2015, *ApJ*, 809, 147
- Heckman, T. M. & Borthakur, S. 2016, *ApJ*, 822, 9
- Henry, A., Scarlata, C., Martin, C. L., & Erb, D. 2015, *ApJ*, 809, 19
- Herenz, E. C., Gruyters, P., Orlitova, I., et al. 2016, *A&A*, 587, A78
- Hjorth, J., Malesani, D., Jakobsson, P., et al. 2012, *ApJ*, 756, 187
- Hjorth, J., Sollerman, J., Möller, P., et al. 2003, *Nature*, 423, 847
- Hunt, L. K., Palazzi, E., Michałowski, M. J., et al. 2014, *A&A*, 565, A112
- Hunter, D. A., Ficut-Vicas, D., Ashley, T., et al. 2012, *AJ*, 144, 134
- Izotov, Y. I., Thuan, T. X., & Guseva, N. G. 2007, *ApJ*, 671, 1297
- Izzo, L., de Ugarte Postigo, A., Maeda, K., et al. 2019, *Nature*, 565, 324
- Izzo, L., Thöne, C. C., Schulze, S., et al. 2017, *MNRAS*, 472, 4480
- James, B. L., Tsamis, Y. G., & Barlow, M. J. 2010, *MNRAS*, 401, 759
- James, B. L., Tsamis, Y. G., Barlow, M. J., Walsh, J. R., & Westmoquette, M. S. 2013, *MNRAS*, 428, 86
- James, B. L., Tsamis, Y. G., Barlow, M. J., et al. 2009, *MNRAS*, 398, 2
- Japelj, J., Vergani, S. D., Salvaterra, R., et al. 2018, *A&A*, 617, A105
- Johnson, M., Hunter, D. A., Oh, S.-H., et al. 2012, *AJ*, 144, 152
- Kann, D. A., Klose, S., & Zeh, A. 2006, *ApJ*, 641, 993
- Kann, D. A., Klose, S., Zhang, B., et al. 2010, *ApJ*, 720, 1513
- Kelly, P. L., Kirshner, R. P., & Pahre, M. 2008, *ApJ*, 687, 1201
- Kewley, L. J., Brown, W. R., Geller, M. J., Kenyon, S. J., & Kurtz, M. J. 2007, *AJ*, 133, 882
- Kocevski, D., Modjaz, M., Bloom, J. S., et al. 2007, *ApJ*, 663, 1180
- Koleva, M., De Rijcke, S., Zeilinger, W. W., et al. 2014, *MNRAS*, 441, 452
- Krühler, T., Kuncarayakti, H., Schady, P., et al. 2017, *A&A*, 602, A85
- Kumari, N., James, B. L., & Irwin, M. J. 2017, *MNRAS*, 470, 4618
- Le Floch, E., Duc, P. A., Mirabel, I. F., et al. 2002, *ApJ*, 581, L81
- Lee, J. C., Kennicutt, Jr., R. C., Funes, S. J. J. G., Sakai, S., & Akiyama, S. 2009, *ApJ*, 692, 1305
- Leloudas, G., Schulze, S., Krühler, T., et al. 2015, *MNRAS*, 449, 917
- Levesque, E. M., Berger, E., Kewley, L. J., & Bagley, M. M. 2010a, *AJ*, 139, 694
- Levesque, E. M., Berger, E., Soderberg, A. M., & Chornock, R. 2011, *ApJ*, 739, 23
- Levesque, E. M., Kewley, L. J., Berger, E., & Zahid, H. J. 2010b, *AJ*, 140, 1557
- Li, L.-X. 2007, *MNRAS*, 375, 240
- Lipkin, Y. M., Ofek, E. O., Gal-Yam, A., et al. 2004, *ApJ*, 606, 381
- Lofthouse, E. K., Houghton, R. C. W., & Kaviraj, S. 2017, *MNRAS*, 471, 2311
- Lyman, J. D., Levan, A. J., Tanvir, N. R., et al. 2017, *MNRAS*, 467, 1795
- Maeda, K., Kawabata, K., Tanaka, M., et al. 2007, *ApJ*, 658, L5
- Maek, K., Buat, V., Roehly, Y., et al. 2018, *A&A*, 620, A50
- Malesani, D., Tagliaferri, G., Chincarini, G., et al. 2004, *ApJ*, 609, L5
- Mannucci, F., Cresci, G., Maiolino, R., Marconi, A., & Gnerucci, A. 2010, *MNRAS*, 408, 2115
- Margutti, R., Chincarini, G., Covino, S., et al. 2007, *A&A*, 474, 815
- Marino, R. A., Rosales-Ortega, F. F., Sánchez, S. F., et al. 2013, *A&A*, 559, A114
- Martin, C. L. 2006, *ApJ*, 647, 222
- Maseda, M. V., van der Wel, A., Rix, H.-W., et al. 2014, *ApJ*, 791, 17
- Matheson, T., Garnavich, P. M., Stanek, K. Z., et al. 2003, *ApJ*, 599, 394
- Mazzali, P. A., Deng, J., Nomoto, K., et al. 2006a, *Nature*, 442, 1018
- Mazzali, P. A., Deng, J., Pian, E., et al. 2006b, *ApJ*, 645, 1323
- Mazzali, P. A., Foley, R. J., Deng, J., et al. 2007, *ApJ*, 661, 892
- McQuinn, K. B. W., Skillman, E. D., Cannon, J. M., et al. 2010, *ApJ*, 724, 49
- Mesler, R. A. & Pihlström, Y. M. 2013, *ApJ*, 774, 77
- Michałowski, M. J., Gentile, G., Hjorth, J., et al. 2015, *A&A*, 582, A78
- Michałowski, M. J., Kamble, A., Hjorth, J., et al. 2012, *ApJ*, 755, 85
- Michałowski, M. J., Xu, D., Stevens, J., et al. 2018, *A&A*, 616, A169
- Miller, S. H., Ellis, R. S., Sullivan, M., et al. 2012, *ApJ*, 753, 74
- Mirabal, N., Halpern, J. P., An, D., Thorstensen, J. R., & Terndrup, D. M. 2006, *ApJ*, 643, L99
- Mirabal, N., Halpern, J. P., & O'Brien, P. T. 2007, *ApJ*, 661, L127
- Modjaz, M., Stanek, K. Z., Garnavich, P. M., et al. 2006, *ApJ*, 645, L21
- Moiseev, A. V. & Lozinskaya, T. A. 2012, *MNRAS*, 423, 1831
- Newman, S. F., Shapiro Griffin, K., Genzel, R., et al. 2012, *ApJ*, 752, 111
- Nicholls, D. C., Dopita, M. A., Sutherland, R. S., et al. 2014, *ApJ*, 786, 155
- Noll, S., Burgarella, D., Giovannoli, E., et al. 2009, *A&A*, 507, 1793
- Olivares E., F., Greiner, J., Schady, P., et al. 2012, *A&A*, 539, A76
- Olmo-García, A., Sánchez Almeida, J., Muñoz-Tuñón, C., et al. 2017, *ApJ*, 834, 181
- Östlin, G., Amram, P., Bergvall, N., et al. 2001, *A&A*, 374, 800
- Östlin, G., Marquart, T., Cumming, R. J., et al. 2015, *A&A*, 583, A55
- Östlin, G., Zackrisson, E., Sollerman, J., Mattila, S., & Hayes, M. 2008, *MNRAS*, 387, 1227
- Ovaldsen, J. E., Jaunsen, A. O., Fynbo, J. P. U., et al. 2007, *ApJ*, 662, 294
- Palmerio, J. T., Vergani, S. D., Salvaterra, R., et al. 2019, *A&A*, 623, A26
- Pei, Y. C. 1992, *ApJ*, 395, 130
- Pérez-Gallego, J., Guzmán, R., Castillo-Morales, A., et al. 2011, *MNRAS*, 418, 2350
- Perley, D. A. & Taggart, K. 2017, *GRB Coordinates Network*, Circular Service, No. 22194, #1 (2017), 22194
- Perley, D. A., Tanvir, N. R., Hjorth, J., et al. 2016, *ApJ*, 817, 8
- Peters, C., van der Horst, A. J., Chomiuk, L., et al. 2019, *ApJ*, 872, 28
- Pian, E., Mazzali, P. A., Masetti, N., et al. 2006, *Nature*, 442, 1011
- Planck Collaboration, Aghanim, N., Akrami, Y., et al. 2020, *A&A*, 641, A6
- Prochaska, J. X., Bloom, J. S., Chen, H.-W., et al. 2004, *ApJ*, 611, 200
- Rodríguez del Pino, B., Arribas, S., Piqueras López, J., Villar-Martín, M., & Colina, L. 2019, *MNRAS*, 486, 344
- Rupke, D. 2018, *Galaxies*, 6, 138
- Sakamoto, T., Lamb, D. Q., Graziani, C., et al. 2004, *ApJ*, 602, 875

- Sánchez Almeida, J., Elmegreen, B. G., Muñoz-Tuñón, C., et al. 2015, *ApJ*, 810, L15
- Savaglio, S., Rau, A., Greiner, J., et al. 2012, *MNRAS*, 420, 627
- Sazonov, S. Y., Lutovinov, A. A., & Sunyaev, R. A. 2004, *Nature*, 430, 646
- Schroetter, I., Bouché, N., Wendt, M., et al. 2016, *ApJ*, 833, 39
- Schulze, S., Krühler, T., Leloudas, G., et al. 2018, *MNRAS*, 473, 1258
- Schulze, S., Malesani, D., Cucchiara, A., et al. 2014, *A&A*, 566, A102
- Soderberg, A. M., Kulkarni, S. R., Berger, E., et al. 2004, *ApJ*, 606, 994
- Soderberg, A. M., Kulkarni, S. R., Fox, D. B., et al. 2005, *ApJ*, 627, 877
- Soderberg, A. M., Kulkarni, S. R., Nakar, E., et al. 2006, *Nature*, 442, 1014
- Sollerman, J., Janssen, A. O., Fynbo, J. P. U., et al. 2006, *A&A*, 454, 503
- Stanek, K. Z., Matheson, T., Garnavich, P. M., et al. 2003, *ApJ*, 591, L17
- Starling, R. L. C., Page, K. L., Pe'Er, A., Beardmore, A. P., & Osborne, J. P. 2012, *MNRAS*, 427, 2950
- Starling, R. L. C., Wiersema, K., Levan, A. J., et al. 2011, *MNRAS*, 411, 2792
- Svensson, K. M., Levan, A. J., Tanvir, N. R., Fruchter, A. S., & Strolger, L.-G. 2010, *MNRAS*, 405, 57
- Swaters, R. A., Sancisi, R., van Albada, T. S., & van der Hulst, J. M. 2009, *A&A*, 493, 871
- Symeonidis, M., Oates, S. R., de Pasquale, M., et al. 2014, *MNRAS*, 443, L124
- Tanga, M., Krühler, T., Schady, P., et al. 2018, *A&A*, 615, A136
- Tanner, R., Cecil, G., & Heitsch, F. 2017, *ApJ*, 843, 137
- Telles, E., Thuan, T. X., Izotov, Y. L., & Carrasco, E. R. 2014, *A&A*, 561, A64
- Thomsen, B., Hjorth, J., Watson, D., et al. 2004, *A&A*, 419, L21
- Thöne, C. C., Campana, S., Lazzati, D., et al. 2011, *MNRAS*, 414, 479
- Thöne, C. C., Christensen, L., Prochaska, J. X., et al. 2014, *MNRAS*, 441, 2034
- Thöne, C. C., Fynbo, J. P. U., Östlin, G., et al. 2008, *ApJ*, 676, 1151
- Thöne, C. C., Greiner, J., Savaglio, S., & Jehin, E. 2007, *ApJ*, 671, 628
- Toma, K., Ioka, K., Sakamoto, T., & Nakamura, T. 2007, *ApJ*, 659, 1420
- Urata, Y., Huang, K., Yamazaki, R., & Sakamoto, T. 2015, *ApJ*, 806, 222
- van Zee, L., Skillman, E. D., & Salzer, J. J. 1998, *AJ*, 116, 1186
- Vanderspek, R., Crew, G., Doty, J., et al. 2003, *GRB Coordinates Network*, 1997
- Veilleux, S., Cecil, G., & Bland-Hawthorn, J. 2005, *ARA&A*, 43, 769
- Verbeke, R., De Rijcke, S., Koleva, M., et al. 2014, *MNRAS*, 442, 1830
- Wainwright, C., Berger, E., & Penprase, B. E. 2007, *ApJ*, 657, 367
- Watson, D., French, J., Christensen, L., et al. 2011, *ApJ*, 741, 58
- Waxman, E., Mészáros, P., & Campana, S. 2007, *ApJ*, 667, 351
- Westmoquette, M. S., Exter, K. M., Smith, L. J., & Gallagher, J. S. 2007, *MNRAS*, 381, 894
- Westmoquette, M. S., Gallagher, J. S., Smith, L. J., et al. 2009a, *ApJ*, 706, 1571
- Westmoquette, M. S., Smith, L. J., Gallagher, III, J. S., et al. 2009b, *ApJ*, 696, 192
- Wiersema, K., Savaglio, S., Vreeswijk, P. M., et al. 2007, *A&A*, 464, 529
- Wiseman, P., Perley, D. A., Schady, P., et al. 2017, *A&A*, 607, A107
- Wood, C. M., Tremonti, C. A., Calzetti, D., et al. 2015, *MNRAS*, 452, 2712
- Woosley, S. E. & Heger, A. 2006, *ApJ*, 637, 914
- Yang, H., Malhotra, S., Gronke, M., et al. 2017, *ApJ*, 844, 171
- Yang, Y., Flores, H., Hammer, F., et al. 2008, *A&A*, 477, 789
- Yin, S. Y., Liang, Y. C., Hammer, F., et al. 2007, *A&A*, 462, 535
- Zabl, J., Bouché, N. F., Schroetter, I., et al. 2020, *MNRAS*, 492, 4576
- Zhao, Y., Gu, Q., & Gao, Y. 2011, *AJ*, 141, 68

Appendix A: Information on the GRBs of the individual host galaxies

Appendix A.1: GRB 020903

GRB 020903 ($z = 0.2506 \pm 0.0003$, Bersier et al. 2006) was a soft X-ray flash (XRF) (Sakamoto et al. 2004) and belongs to the class of low-luminosity GRBs with an E_{iso} of 1.1×10^{49} ergs. The afterglow showed an initial rise during the first few hours (Bersier et al. 2006; Urata et al. 2015), however, data on the optical afterglow is sparse while the radio afterglow resembles regular afterglows in brightness and temporal behavior (Soderberg et al. 2004). Soderberg et al. (2005) and Bersier et al. (2006) detected a SN with spectra similar to SN1998bw but 0.5–0.6 mag fainter.

Appendix A.2: GRB 030329

GRB 030329 ($z = 0.16867 \pm 0.00001$, Thöne et al. 2007), detected by the HETE-2 satellite (Vanderspek et al. 2003), represents the first spectroscopic association of a broad-line Type Ic SN with a cosmological long GRB, SN 2003dh (Stanek et al. 2003; Hjorth et al. 2003; Matheson et al. 2003). It is still the GRB with the largest optical afterglow follow-up data set (e.g., Lipkin et al. 2004; Kann et al. 2006) and its radio afterglow had been observed for over 13 years (Mesler & Pihlström 2013; Peters et al. 2019). With an E_{iso} 1.74×10^{52} erg (Kann et al. 2010) it is also one of the most energetic GRBs at low redshift.

Appendix A.3: GRB 031203

GRB 031203 ($z = 0.10536 \pm 0.00007$, Margutti et al. 2007) was detected by INTEGRAL and is part of the nearby low-luminosity GRB population (Sazonov et al. 2004; Soderberg et al. 2004). It had a very weak afterglow and a bright but otherwise standard accompanying BL Type Ic SN 2003lw (Malesani et al. 2004; Gal-Yam et al. 2004; Thomsen et al. 2004; Cobb et al. 2004). The host galaxy has been extensively studied (e.g., Prochaska et al. 2004; Margutti et al. 2007; Watson et al. 2011; Guseva et al. 2011; Symeonidis et al. 2014).

Appendix A.4: GRB 050826

GRB 050826 ($z = 0.296 \pm 0.001$, Mirabal et al. 2007) was a relatively low-luminosity GRB behind significant Galactic extinction. Its redshift was not reported until several months later (Halpern & Mirabal 2006), and follow-up was very sparse (Mirabal et al. 2007). No SN follow-up has been reported.

Appendix A.5: GRB 060218

This very low redshift burst ($z = 0.03342 \pm 0.00002$, Pian et al. 2006) was an X-ray flash (XRF) with a very long duration of ~ 2100 s, and is another low-luminosity GRB (Soderberg et al. 2006). It may be associated with a magnetar (Mazzali et al. 2006a; Toma et al. 2007) and showed a peculiar afterglow with an additional thermal component in the X-rays and in the optical (Campana et al. 2006; Starling et al. 2012), interpreted as shock-breakout of the SN from the star (Campana et al. 2006; Waxman et al. 2007; Li 2007). The associated broad-line Type Ic SN 2006aj was extensively studied (Pian et al. 2006; Modjaz et al. 2006; Mirabal et al. 2006; Sollerman et al. 2006; Cobb et al. 2006; Ferrero et al. 2006; Gorosabel et al. 2006; Mazzali et al. 2007; Kocevski et al. 2007; Maeda et al. 2007).

Appendix A.6: GRB 100316D

GRB 100316D was a very low redshift ($z = 0.0592 \pm 0.0001$, Bufano et al. 2012), long duration ($T_{90} = 1500$ s), subluminous XRF with a soft prompt emission spectrum and a thermal component in X-rays (Starling et al. 2012). Due to some confusion of the optical counterpart with bright star-forming regions in the host during the first days, there is very little information on the actual afterglow. However, the accompanying broad-lined Type Ic SN 2010dh was well-studied. (Chornock et al. 2010; Cano et al. 2011a; Olivares E. et al. 2012; Bufano et al. 2012).

Appendix B: Reanalysis of the metallicity of the host of GRB 050826

Levesque et al. (2010b) cite a supersolar metallicity based on long-slit spectra from LRIS/Keck. The FLAMES spectrum shows a low significance emission excess at the position of the [N II], however, at that metallicity, [N II] λ 6585 should be strong. Assuming the same line width for H α and [N II], we derive a $3\text{-}\sigma$ limit of [N II]/H α < 0.25 , corresponding to a metallicity limit of $12+\log(\text{O}/\text{H}) < 8.45$, in clear disagreement with the value in Levesque et al. (2010b). To investigate this further, we analyzed the original long-slit spectrum from Levesque et al. (2010b) (D. Perley, priv. comm.) taken with a 1" slit at an orientation of 343 degrees (almost N-S), hence covering most of the galaxy. In this spectrum we measure a ratio [N II]/H α of 0.2, in good agreement with our measurements in the FLAMES spectrum. The metallicity in Levesque et al. (2010b) was derived using the R₂₃ parameter. However, the authors use the upper branch of this two-valued metallicity calibrator, which in this case is the wrong branch. Since the flux ratio from both datasets are consistent, the metallicity value stated in Levesque et al. (2010b) is incorrect.

Appendix C: SED fit with CIGALE

Using photometric data from the literature (see Tables C.2 and C.3) we perform a Spectral Energy Distribution (SED) analysis of the host galaxy of the FLAMES sample with CIGALE² (Burgarella et al. 2005; Noll et al. 2009; Boquien et al. 2019) using its 2020 version. We consider a delayed star-formation history with an age for the main stellar population in the galaxies ranging from 500 Myr to 12 Gyr and an age range for the recent SF burst of 20–50 Myr to keep the computational effort at a reasonable degree. The delayed SFR function is based on Malek et al. (2018), which is again building on the considerations of (eq. 3 in Ciesla et al. 2015). This approach gives better estimates for the mass-weighted SFR than the case with a simple or double exponential SFR. We use an Initial Mass Function (IMF) as described in Chabrier (2003) and a stellar population model from Bruzual & Charlot (2003), assuming a metallicity Z with values of 0.008, 0.02 or 0.05.

Dust attenuation is treated differently for emission lines and continuum. To model the continuum extinction, we consider the modified Calzetti et al. (2000) attenuation law. The slope δ for continuum extinction curve $k_{\lambda} = A(\lambda)/E(B-V)$ with $k_{\lambda} \propto \lambda^{\delta}$ was left to vary from -0.6 to 0.6 in steps of 0.2 (see Boquien et al. (2019, eq. 8)). For the attenuation of the emission lines we use a MW (Cardelli et al. 1989), LMC and SMC (Pei 1992) extinction law with $R_V = 3.1, 2.93$ and 3.16 respectively. The color excess between emission lines and continuum attenuation, measured by the ratio $f = E(B-V)_{\text{cont.}}/E(B-V)_{\text{em.lines}}$ was determined to be 0.44,

² <https://cigale.lam.fr/>

hence the younger population (causing the emission lines) has higher extinction than the older population. We also take into account the light from stars re-emitted in the IR by dust by using the Dale et al. (2014) models. When we have both mid- and far-infrared photometry for some hosts, we adopt the slope for the dust mass heated by the radiation field to be $\alpha = 2$, as found in Dale & Helou (2002). When FIR data are not available, α_{IR} can vary from 1 to 3, with steps of 0.5. No AGN component has been added to the analysis. For the final results we adopt the results fitting an SMC SED to the data.

Table C.1. Results for the SED fitting

GRB	z	$\log_{10}\text{SFR}$ $M_{\odot} \text{ y}^{-1}$	$\log_{10}M^*$ M_{\odot}	A_V mag	$E(B-V)$ mag	Z	Reduced - χ^2	sSFR Gyr^{-1}
GRB100316D	0.0591	$-0.16^{+0.02}_{-0.03}$	$9.39^{+0.07}_{-0.08}$	0.08 ± 0.02	0.05 ± 0.00	0.0080	0.78	0.28 ± 0.05
GRB060218	0.0331	$-0.91^{+0.05}_{-0.06}$	$7.40^{+0.06}_{-0.07}$	1.09 ± 0.18	0.48 ± 0.11	0.0080	1.87	5.00 ± 0.98
GRB050826	0.296	$0.88^{+0.40}_{-0.30}$	$9.99^{+0.25}_{-0.65}$	0.86 ± 0.67	0.47 ± 0.33	0.0080	0.03	0.77 ± 1.30
GRB031203	0.1055	$0.46^{+0.04}_{-0.05}$	$8.86^{+0.09}_{-0.12}$	0.59 ± 0.08	0.33 ± 0.05	0.0080	3.73	3.94 ± 1.03
GRB030329	0.169	$-0.80^{+0.13}_{-0.18}$	$7.70^{+0.12}_{-0.17}$	0.33 ± 0.24	0.16 ± 0.10	0.0200	1.85	3.17 ± 1.52
GRB020903	0.2506	$0.25^{+0.18}_{-0.33}$	$8.94^{+0.21}_{-0.40}$	0.25 ± 0.26	0.13 ± 0.14	0.0500	0.60	2.05 ± 1.64
GRB100316D	0.0591	$-0.16^{+0.02}_{-0.03}$	$9.39^{+0.07}_{-0.08}$	0.07 ± 0.02	0.05 ± 0.00	0.0080	0.78	0.28 ± 0.05
GRB060218	0.0331	$-0.91^{+0.05}_{-0.06}$	$7.40^{+0.06}_{-0.07}$	1.09 ± 0.18	0.49 ± 0.11	0.0080	1.93	4.97 ± 1.00
GRB050826	0.296	$0.86^{+0.37}_{-0.43}$	$9.98^{+0.25}_{-0.62}$	0.85 ± 0.65	0.47 ± 0.32	0.0080	0.03	0.75 ± 1.18
GRB031203	0.1055	$0.46^{+0.04}_{-0.04}$	$8.86^{+0.09}_{-0.12}$	0.58 ± 0.08	0.33 ± 0.05	0.0080	3.70	4.02 ± 1.05
GRB030329	0.169	$-0.80^{+0.13}_{-0.18}$	$7.70^{+0.12}_{-0.17}$	0.33 ± 0.24	0.16 ± 0.10	0.0200	1.85	3.17 ± 1.52
GRB020903	0.2506	$0.24^{+0.18}_{-0.30}$	$8.93^{+0.21}_{-0.41}$	0.23 ± 0.24	0.13 ± 0.13	0.0500	0.61	2.00 ± 1.57
GRB100316D	0.0591	$-0.16^{+0.02}_{-0.03}$	$9.39^{+0.07}_{-0.08}$	0.08 ± 0.02	0.05 ± 0.00	0.0080	0.78	0.28 ± 0.05
GRB060218	0.0331	$-0.91^{+0.05}_{-0.06}$	$7.39^{+0.06}_{-0.07}$	1.09 ± 0.18	0.48 ± 0.11	0.0080	1.88	5.00 ± 0.98
GRB050826	0.296	$0.88^{+0.39}_{-0.32}$	$9.99^{+0.25}_{-0.64}$	0.86 ± 0.67	0.47 ± 0.33	0.0080	0.03	0.77 ± 1.29
GRB031203	0.1055	$0.46^{+0.04}_{-0.05}$	$8.86^{+0.09}_{-0.12}$	0.59 ± 0.08	0.32 ± 0.05	0.0080	3.73	3.96 ± 1.04
GRB030329	0.169	$-0.80^{+0.13}_{-0.18}$	$7.70^{+0.12}_{-0.17}$	0.33 ± 0.24	0.16 ± 0.10	0.0200	1.85	3.17 ± 1.52
GRB020903	0.2506	$0.25^{+0.18}_{-0.33}$	$8.94^{+0.21}_{-0.40}$	0.25 ± 0.26	0.13 ± 0.14	0.0500	0.60	2.05 ± 1.64

Notes. Fits were done with a Milky Way attenuation law, $R_V = 3.1$ (top), Large Magellanic Cloud attenuation law, $R_V = 3.16$ (middle) and Small Magellanic Cloud attenuation law, $R_V = 2.93$

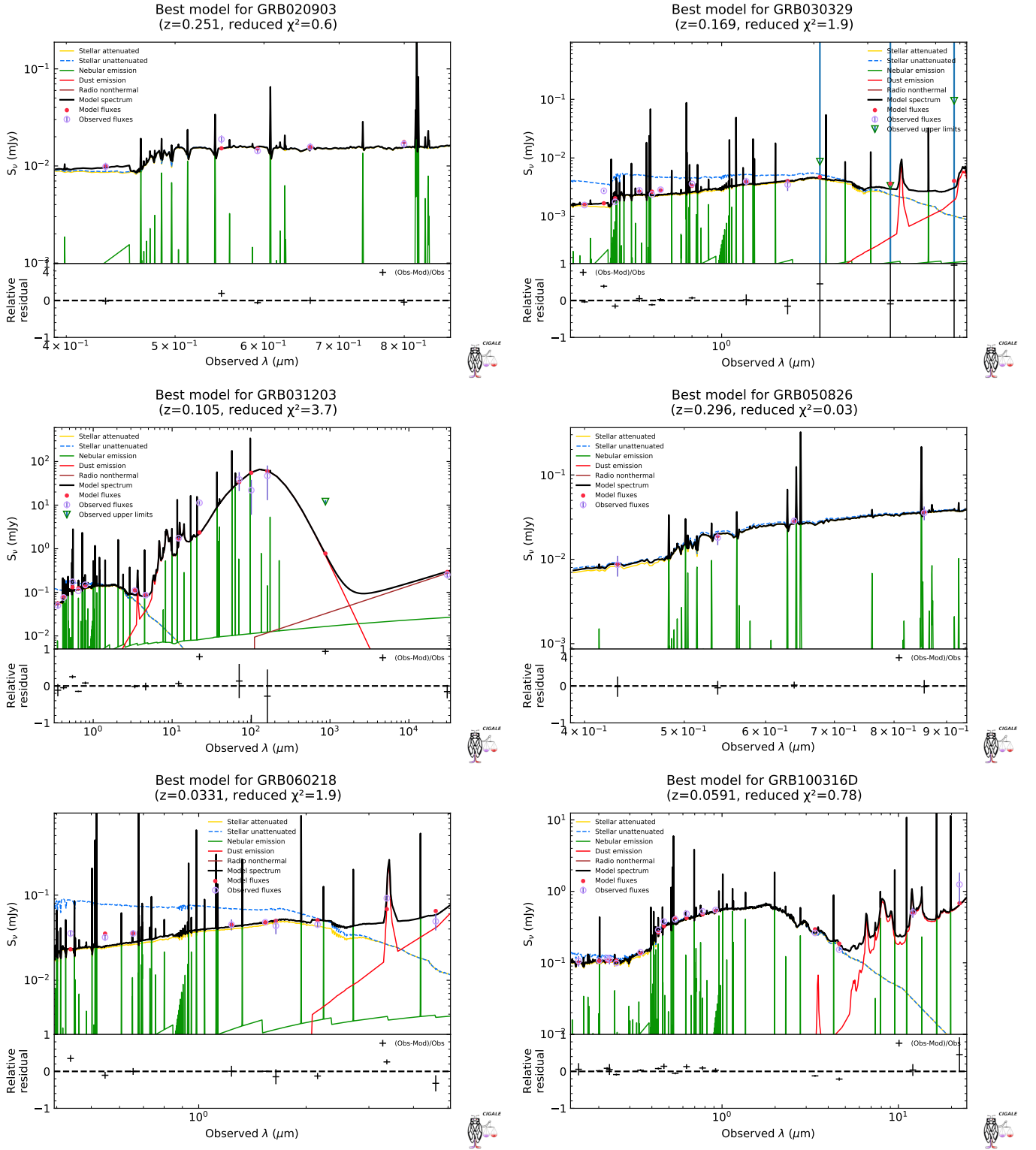


Fig. C.1. CIGALE SED fits of the hosts of GRB 020903, GRB 030329, GRB 031203, GRB 050826, GRB 060218 and GRB 100316D using the photometric data presented in Tab. C.2 and C.3.

Table C.2. Photometry used for the SED fitting for all hosts except the one of GRB 031203.

Band	Instrument	AB Magnitude	Reference
GRB 020903			
I	CTIO/MosaicII	20.83 ± 0.10	Bersier et al. (2006)
R	CTIO/MosaicII	20.91 ± 0.10	Bersier et al. (2006)
F606W	HST/ACS	21.01 ± 0.05	Wainwright et al. (2007)
V	Danish 1.54 Telescope	20.71 ± 0.10	Bersier et al. (2006)
B	Danish 1.54 Telescope	21.41 ± 0.10	Bersier et al. (2006)
GRB 030329			
IRAC3	<i>Spitzer</i> /IRAC	> 18.96	Svensson et al. (2010)
IRAC1	<i>Spitzer</i> /IRAC	> 22.59	Svensson et al. (2010)
K'	CAHA/Omega2000	> 21.56	Gorosabel, J. et al. (2005)
H	CAHA/Omega2000	22.54 ± 0.24	Gorosabel, J. et al. (2005)
J	CAHA/Omega2000	22.40 ± 0.16	Gorosabel, J. et al. (2005)
F814W	HST/ACS	22.71 ± 0.05	Wainwright et al. (2007)
C4	CAHA/BUSCA	22.51 ± 0.04	Gorosabel, J. et al. (2005)
R	CAHA/MOSCA	22.81 ± 0.04	Gorosabel, J. et al. (2005)
C3	CAHA/BUSCA	22.76 ± 0.04	Gorosabel, J. et al. (2005)
F606W	HST/ACS	22.81 ± 0.05	Wainwright et al. (2007)
V	CAHA/MOSCA	22.78 ± 0.10	Gorosabel, J. et al. (2005)
B	CAHA/MOSCA	23.27 ± 0.07	Gorosabel, J. et al. (2005)
F435W	HST/ACS	24.11 ± 0.10	Wainwright et al. (2007)
C2	CAHA/BUSCA	22.80 ± 0.05	Gorosabel, J. et al. (2005)
U	CAHA/MOSCA	23.35 ± 0.10	Gorosabel, J. et al. (2005)
C1	CAHA/BUSCA	23.41 ± 0.03	Gorosabel, J. et al. (2005)
GRB 050826			
I	Danish 1.54 Telescope	20.02 ± 0.20	Ovaldsen et al. (2007)
R	Danish 1.54 Telescope	20.26 ± 0.10	Ovaldsen et al. (2007)
V	Danish 1.54 Telescope	20.76 ± 0.20	Ovaldsen et al. (2007)
B	Danish 1.54 Telescope	21.56 ± 0.30	Ovaldsen et al. (2007)
	Not included in fit		
R	Unknown	20.89 ± 0.06	Ovaldsen et al. (2007)
V	Unknown	20.30 ± 0.05	Ovaldsen et al. (2007)
GRB 060218			
Ks	VLT/ISAAC	19.77 ± 0.09	Hjorth et al. (2012)
H	2MASS	19.80 ± 0.22	Kocevski et al. (2007)
J	2MASS	19.76 ± 0.16	Kocevski et al. (2007)
R _c	SUBARU/FOCAS	20.03 ± 0.10	Maeda et al. (2007)
V	SUBARU/FOCAS	20.14 ± 0.10	Maeda et al. (2007)
B	SUBARU/FOCAS	20.02 ± 0.10	Maeda et al. (2007)
F160W	HST/WFC3	19.70 ± 0.01	Lyman et al. (2017)
	Not included in fit		
F160W	HST/WFC3	19.611 ± 0.003	Blanchard et al. (2016)
GRB 100316D			
WISE4	WISE	16.16 ± 0.51	ALLWISE
WISE3	WISE	17.13 ± 0.17	ALLWISE
WISE2	WISE	18.44 ± 0.05	ALLWISE
WISE1	WISE	17.86 ± 0.03	ALLWISE
z'	Gemini/GMOS-South	17.06 ± 0.06	Cano et al. (2011b)
i'	Gemini/GMOS-South	17.10 ± 0.06	Cano et al. (2011b)
r'	Gemini/GMOS-South	17.18 ± 0.07	Cano et al. (2011b)
UVOT V	<i>Swift</i> /UVOT	17.38 ± 0.03	Starling et al. (2011)
g'	Gemini/GMOS-South	17.46 ± 0.08	Cano et al. (2011b)
UVOT B	<i>Swift</i> /UVOT	17.75 ± 0.03	Starling et al. (2011)
UVOT U	<i>Swift</i> /UVOT	18.53 ± 0.03	Starling et al. (2011)
UVOT UVW1	<i>Swift</i> /UVOT	18.91 ± 0.03	Starling et al. (2011)
UVOT UVM2	<i>Swift</i> /UVOT	18.73 ± 0.03	Starling et al. (2011)
UVOT UVW2	<i>Swift</i> /UVOT	18.82 ± 0.02	Starling et al. (2011)

Notes. Magnitudes are in the AB system and have been corrected for Galactic extinction.

Table C.3. GRB 031203 host galaxy photometry.

Band	Instrument	Flux mJy	Reference
1.39 GHz	ATCA	0.191 ± 0.037	Watson et al. (2011)
3.45 GHz	APEX/LABOCA	< 0.012	Watson et al. (2011)
160 μ	Herschel/PACS	47.000 ± 34.000	Symeonidis et al. (2014)
100 μ	Herschel/PACS	22.000 ± 16.000	Symeonidis et al. (2014)
70 μ	Herschel/PACS	39.000 ± 18.000	Symeonidis et al. (2014)
WISE4	WISE	11.300 ± 1.000	Symeonidis et al. (2014)
WISE3	WISE	1.740 ± 0.120	Symeonidis et al. (2014)
WISE2	WISE	0.086 ± 0.009	Symeonidis et al. (2014)
WISE1	WISE	0.110 ± 0.005	Symeonidis et al. (2014)
I	VLT/FORS2	0.149 ± 0.005	Mazzali et al. (2006b)
R	VLT/FORS2	0.108 ± 0.002	Mazzali et al. (2006b)
V	VLT/FORS2	0.174 ± 0.008	Margutti et al. (2007)
B	VLT/FORS1	0.076 ± 0.004	Margutti et al. (2007)
U	VLT/FORS1	0.050 ± 0.008	Margutti et al. (2007)

Notes. For this host we list flux densities in mili-Jansky instead of magnitudes. Fluxes have been corrected for Galactic extinction.